Mechanical Feedback and Robustness of Apical Constrictions in Drosophila Embryo Ventral Furrow Formation

Michael C. Holcomb[1†], Guo-Jie Jason Gao[2], Mahsa Servati[1‡], Dylan Schneider[3], Presley K. McNeely[1], Jeffrey H. Thomas[4*], Jerzy Blawzdziewicz[1,3*]

*For correspondence:
jerzy.blawzdziewicz@ttu.edu (JB);
jeffrey.thomas@ttuhsc.edu (JHT)

Present address: †Department of Physics and Geosciences, Angelo State University, 2601 W. Avenue N, San Angelo, TX 76909, USA; ‡School of Health Sciences, Purdue University, 550 Stadium Mall Dr., West Lafayette, IN 47907, USA

[1]Department of Physics and Astronomy, Texas Tech University, Box 41051, Lubbock, TX 79409-1051, USA; [2]Department of Mathematical and Systems Engineering, Shizuoka University, Hamamatsu, Shizuoka 432-8561, Japan; [3]Department of Mechanical Engineering, Texas Tech University, Box 41021, Lubbock, TX 79409-1021, USA; [4]Department of Cell Biology and Biochemistry, Texas Tech University Health Sciences Center, Mail Stop 6540, Lubbock, TX 79430, USA

Abstract The key process giving rise to ventral furrow formation (VFF) in the *Drosophila* embryo is apical (outer side) constriction of cells in the ventral region. A combined effect of the cellular constrictions is a negative spontaneous curvature of the cell layer, which buckles inwards. In our recent paper [Gao et al. (2016). J Phys Condens Matter, 28(41), 414021] we showed that the cell constrictions in the initial phase of VFF produce well-defined cellular constriction chain (CCC) patterns, and we argued that CCC formation is a signature of mechanical signaling that coordinates apical constrictions through tensile stress. In the present study, we provide a statistical comparison between our active granular fluid (AGF) model and time lapses of live embryos. We also demonstrate that CCCs can penetrate regions of reduced constriction probability, and we argue that CCC formation increases robustness of VFF to spatial variation of cell contractility.

Introduction

Previous research efforts to understand morphogenesis have primarily focused on the identification of genetic information and biochemical signals involved in formation of embryonic architecture. In recent years, however, there has emerged compelling evidence that cell communication via mechanical forces is crucial in orchestrating morphogenetic processes (*Mammoto and Ingber, 2010*; *Zhang and Labouesse, 2012*; *Miller and Davidson, 2013*; *Chanet and Martin, 2014*; *Heer and Martin, 2017*; *Hunter and Fernandez-Gonzalez, 2017*; *Gilmour et al., 2017*; *Ladoux and Mége, 2017*). In *Drosophila* gastrulation, mechanical signaling has been shown to be a triggering mechanism for morphogenetic events (*Farge, 2003*; *Brouzés and Farge, 2004*; *Pouille et al., 2009*; *Mitrossilis et al., 2017*; *Weng and Wieschaus, 2016*), and mechanical feedback to be a factor in the coordination of cellular activities in mesoderm primordium (*Gao et al., 2016*). Mechanical feedback is also involved in remodeling subcellular components such as adherens junctions (*Weng and Wieschaus, 2016*) and the supracellular actomyosin meshwork (*Chanet et al., 2017*).

To elucidate the role of mechanical forces and mechanical feedback in embryonic development,
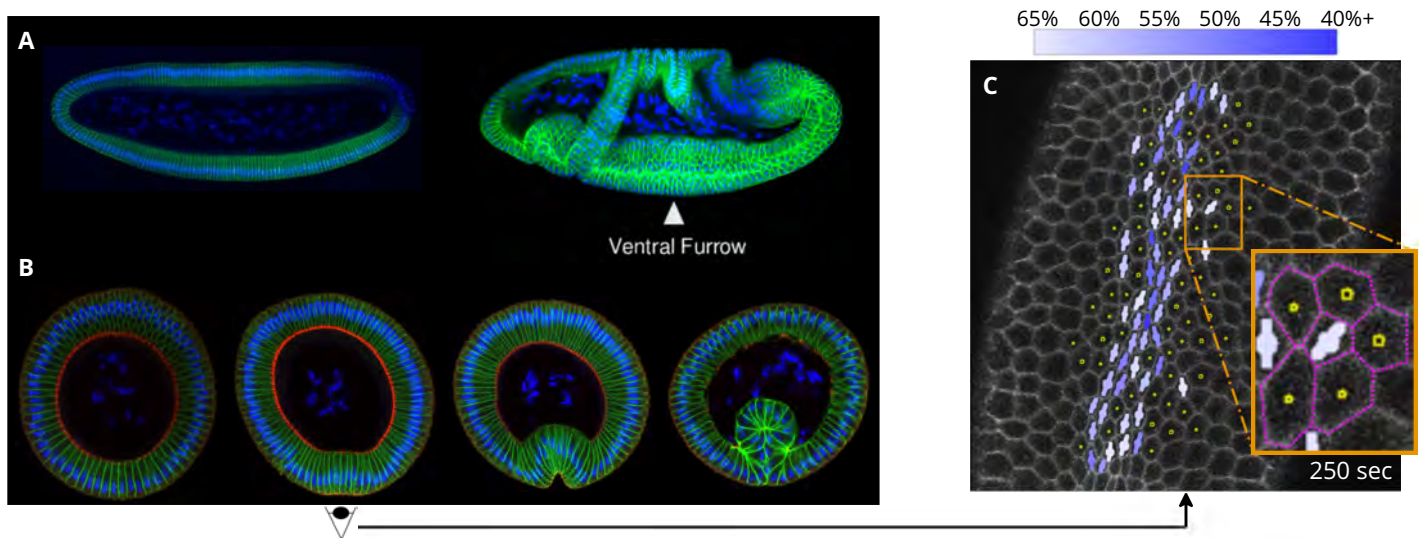
Figure 1. VFF in the *Drosophila* embryo. (**A**) The embryo before and after gastrulation; position of the ventral furrow is indicated. (**B**) Cross-sectional images of fixed embryos, showing the progression of VFF. (**C**) Processed confocal microscopy image of a live Spider-GFP embryo towards the end of the initial slow apical constriction phase of VFF. Constricted cells are indicated by a bar with a circle (bar–circle), where the bar represents the direction and length of the major cell axis, and the size of the circle is proportional to the cell area. Color saturation indicates the degree of constriction, measured by the reduction of the cells minor axis length relative to the reference value (as defined in *Equation 1* and indicated by the color bar). Tracked cells are indicated by the dots. In A, B embryos were heat-methanol fixed, stained with Hoeschst (blue), antibodies to Neurotactin (green), and antibodies to Zipper (myosin heavy chain, red);the images were acquired by confocal microscopy.

₃₉ we have recently analyzed the dynamics of the apical constriction process during the earliest stage
₄₀ of ventral furrow formation (VFF) in the *Drosophila* embryo (*Gao et al., 2016*). During this process,
₄₁ the apical (outer) sides of cells in the ventral region constrict, producing negative spontaneous
₄₂ curvature of the cell layer. Subsequently, the layer buckles inwards as the result of the constriction-
₄₃ induced bending stresses (see *Figure 1* for relevant details of *Drosophila* gastrulation).

₄₄ Our study (*Gao et al., 2016*) showed that cell constrictions during the initial slow phase of VFF are
₄₅ not random uncorrelated events as previously assumed (*Sweeton et al., 1991*). Instead, constricted
₄₆ cell apices form well-defined correlated structures which we termed cellular constriction chains
₄₇ (CCCs). Formation of CCCs (see the highlighted cells in *Figure 1*C, *Figure 2* and *Figure 3*) implies
₄₈ the existence of strong spatial and directional correlations between the constriction events. *Xie*
₄₉ *and Martin* (*2015*) also published evidence that pulsed apical constrictions were not random but
₅₀ correlated with neighboring cells.

₅₁ Based on a qualitative analysis of geometrical patterns of CCCs, we proposed (*Gao et al., 2016*)
₅₂ that CCCs originate from communication between cells via mechanical feedback. To explain this
₅₃ mechanism of CCC formation we have developed a theoretical active granular fluid (AGF) model of
₅₄ the apical surface of the cell monolayer. In this model, the cells (more specifically, their mechanically
₅₅ active apical ends) are treated as mechanically sensitive interacting particles undergoing a stochastic
₅₆ constriction process. The model predicts that if cells react to tensile stress by increasing apical-
₅₇ constriction probability, the constricted cells tend to form chain-like structures similar to CCCs
₅₈ observed *in vivo*.

₅₉ In the present paper, we use the AGF model and live embryo data to quantitatively analyze
₆₀ constriction patterns observed in mesoderm primordium in *Drosophila* embryos. Our aim is twofold.
₆₁ First, we determine statistical features of constricted-cell clusters that can quantitatively distinguish
₆₂ between purely random uncorrelated constriction patterns and those resulting from constrictions
₆₃ correlated by tensile stress. These statistical characteristics, identified using the AGF model, are
₆₄ applied to live embryo data, providing a clear indication that tensile mechanical feedback is an
₆₅ important controlling factor involved in the initial slow phase of apical constrictions during VFF.

Second, to shed light on the biological function of mechanical feedback between constricting cells, we investigate the cellular constriction process in systems with zones of reduced cell capability to constrict. Our AGF simulations demonstrate that coordination of apical constrictions by tensile stress allows CCCs to penetrate or bypass regions of reduced constriction probability, thus rescuing the constriction process. An analysis of constriction patterns in live embryos in which contractile force transmission has locally been reduced using optogenetic techniques (*Guglielmi et al., 2015*) is consistent with our theoretical findings. We thus conclude that mechanical feedback and the associated formation of CCCs aid robustness of the VFF process in the presence of environmental or genetic fluctuations.

Results

Confocal images of the ventral surface of live Spider-GFP embryos show CCCs emerging during the initial slow phase of VFF

Gastrulation in *Drosophila* occurs through a progression of partially concurrent morphogenetic movements that result in the emergence of a complex embryonic architecture depicted in *Figure 1*A. These movements are generated by coordinated activities of nearly identical cells in distinct genetically specified regions established at the early stage of embryonic development as a result of a cascading biochemical pattern formation process (*St Johnston and Nüsslein-Volhard, 1992*; *Riechmann and Ephrussi, 2001*; *Huynh and St Johnston, 2004*; *van Eeden and St Johnston, 1999*).

Here we focus on VFF, the earliest morphogenetic movement in *Drosophila* gastrulation. The VFF process is driven by apical constrictions of cells in the mesoderm primordium, i.e., the band of cells in the ventral region of the embryo that will subsequently undergo epithelial invagination (see the schematic shown in *Figure 4*A). These cells are capable of mechanical activity due to expression of regulatory genes *twist* and *snail* (*Leptin and Grunewald, 1990*; *Leptin, 1991*; *Ip et al., 1994*; *Seher et al., 2007*; *Martin et al., 2009*; *Pouille et al., 2009*). Our study addresses the question whether, beyond genetic regulation, the mesoderm primordium cells communicate via mechanical feedback to coordinate their activities during the VFF process.

As illustrated in *Figure 1*B,C, several distinct VFF phases can be distinguished (*Sweeton et al., 1991*): (1) The early slow phase during which a growing number of mesoderm primordium cells undergo apical constrictions; (2) the fast transition phase, where the remaining cells undergo apical constrictions at the onset of buckling of the cell layer; and (3) the invagination phase during which the ventral furrow forms. The shift from the slow phase of VFF to the fast phase and the subsequent invagination occurs when approximately 40% of cells in the mesoderm primordium have constricted. CCCs emerge during the slow phase (1).

Constriction patterns visualized using minor axis length to identify constricted cells

Development of CCC patterns on the apical surface of the mesoderm primordium is depicted in the confocal images of live Spider-GFP embryos shown in *Figure 1*C, *Figure 2*, and *Figure 3*. We observed that constriction along the minor axis of the cell apex was the critical parameter of apical constriction based on the geometry of the cells. This observation is consistent with the dorsal-ventral (ventral-lateral) bias in apical constriction previously observed (*Martin, 2010*; *Heer et al., 2017*). In these images, the cells are marked as constricted based on their minor axis length (MAL) reduction relative to the reference MAL,

$$r = \lambda/\lambda_{\text{ref}}. \tag{1}$$

Here λ is the MAL of a given cell, and λ_{ref} is its reference value established for each individual cell by averaging over twenty sequential frames before constrictions begin. In *Figure 2*, cells are marked as constricted if their MAL drops below 65% of their reference MAL (i.e., when $r < 0.65 = r_{\text{c}}$). The distribution of the MAL reduction values in the last frame of *Figure 2* is depicted in *Figure 1*C, and constriction patterns for different values of the cutoff parameter r_{c} are presented in *Figure 3*.
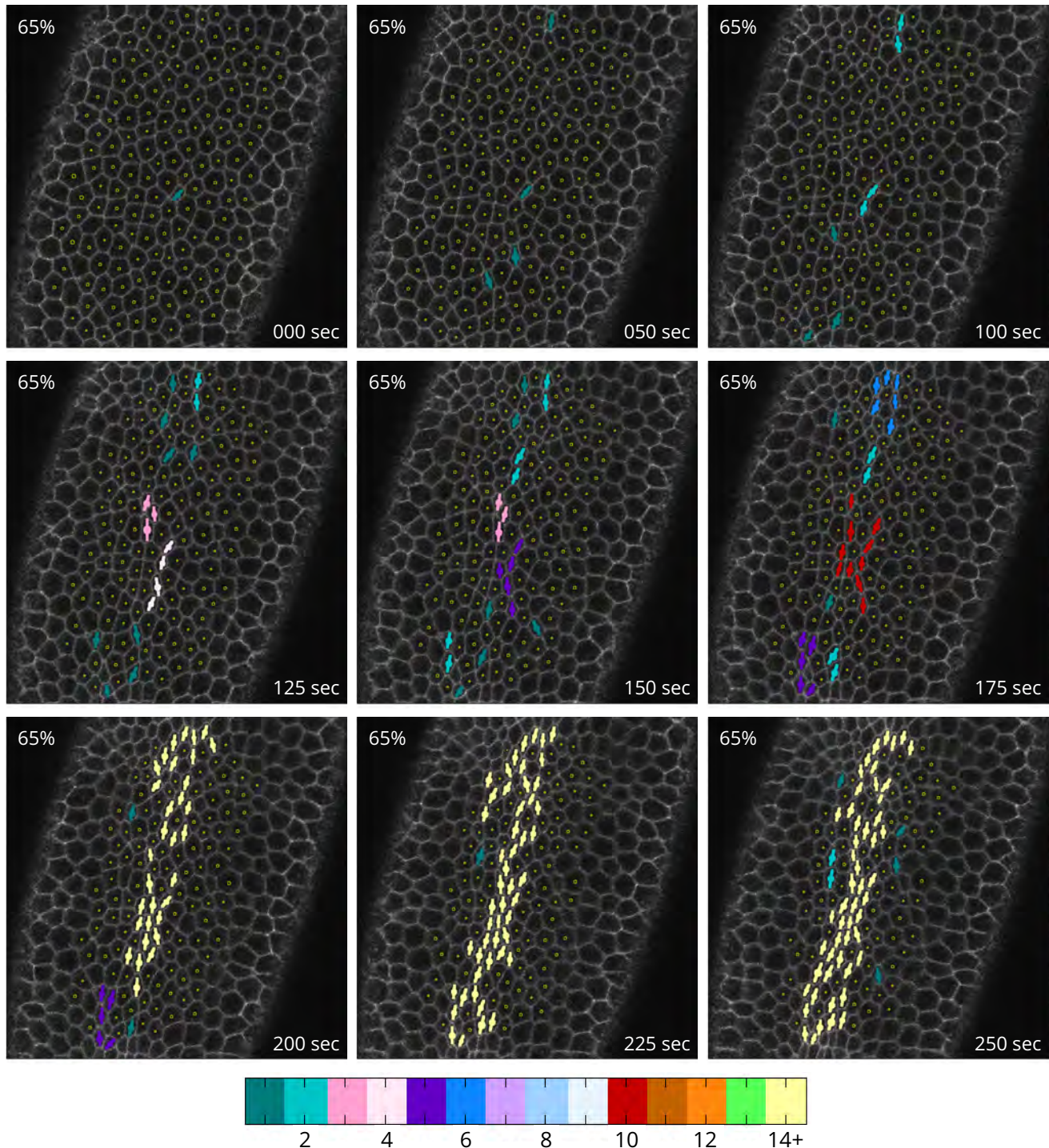
Figure 2. Development of CCCs during the slow apical constriction phase of VFF. The constricted cells in the processed confocal microscopy time lapse images of the underside of a Spider-GFP are marked based on the MAL reduction cutoff value (r_c) of 0.65. The symbols follow the same convention as the one used in *Figure 1*, except that the colors indicate the number of cells, interconnected via shared neighbors, belonging to a single constricted-cell cluster. Cells initially constrict alone, forming singlets; however, they quickly begin to develop elongated chain-like structures, i.e., CCCs. The CCCs grow rapidly and interconnect, eventually forming a network that percolates across the mesoderm primordium along the anteroposterior axis. Many of the marked cells remain constricted across multiple frames, indicating that they are undergoing ratcheted constrictions (*Xie and Martin, 2015*); however, some unratcheted constrictions can also be seen.
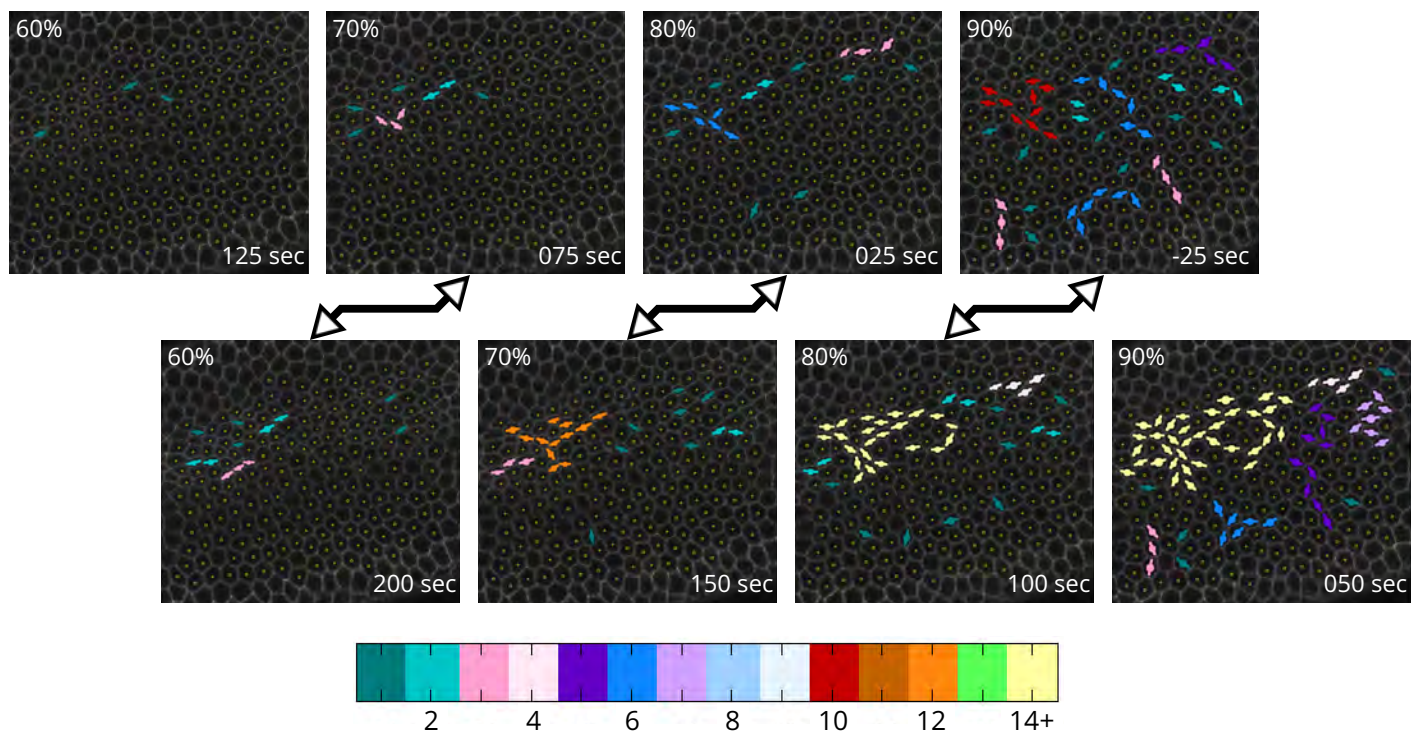
Figure 3. Threshold Comparison. Processed confocal microscopy images of the apical constriction phase of VFF in a single Spider-GFP embryo that have been processed with different MAL reduction threshold values (r_c) for constricted cell identification. Time zero selected as the first frame with $r_c = 0.65$ that has a constricted cell that persists across multiple frames. The symbol convention is the same as the one used in *Figure 2*. Double headed arrows identify frames where CCC development is relatively similar between a stronger r_c and a weaker r_c at an earlier time. Varying r_c does not change the form of the CCCs that are observed and instead shows their different stages of development.
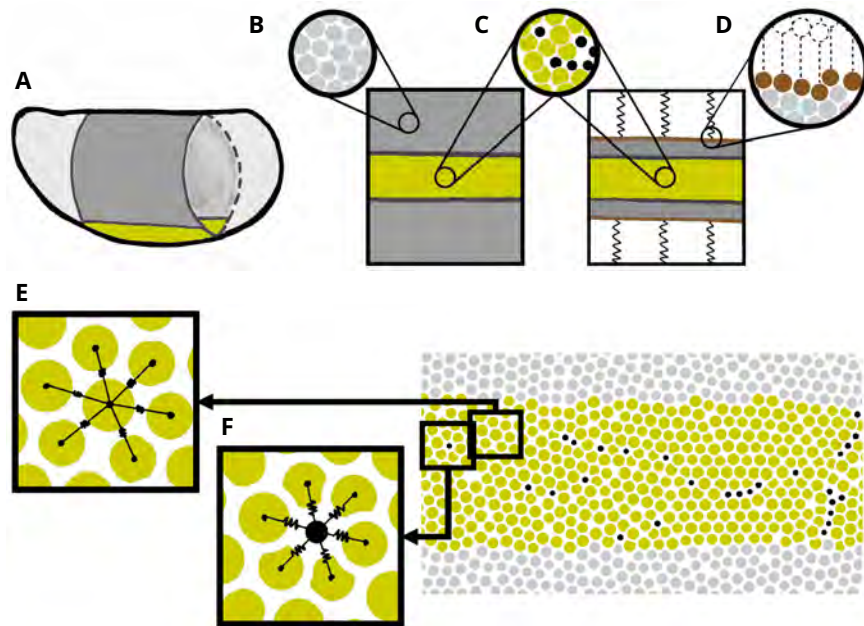
Figure 4. AGF model schematic. (**A**) The model represents the apical surface of the *Drosophila* embryo. Shown in orange is the region of active cells in the mesoderm primordium, where cells undergo apical constrictions during the initial phase of VFF. Inactive cells in the lateral and dorsal regions (shown in gray) do not experience constrictions. Inserts show how cells in both (**B**) inactive and (**C**) active regions are modeled as disks. Insert (**D**) shows how we implicitly model a portion of the inactive region as an effective elastic medium, in the interest of computational efficiency. (**E**) Cells interact with their adjacent neighbors through pairwise elastic potentials. (**F**) Cells maintain the same neighbors even after constriction. Constricted cells are marked in black.

112   According to the results shown in *Figure 2*, the slow phase of VFF begins with individual cells
113 undergoing constrictions without forming any apparent spatial pattern. After this initial stage,
114 CCCs gradually emerge, i.e., elongated chain-like configurations of constricting cells appear in the
115 ventral region. The CCCs begin as doublets or triplets of constricted cells and rapidly grow in length.
116 Expanding CCCs branch and merge, promoting interconnection of the constricted-cell network and
117 eventually leading to percolation of CCCs across the active region.
118   Important insights can be obtained from an analysis of constriction patterns displayed in *Figure 3*
119 using different MAL reduction cutoff values r_c. The comparison of the images show in the bottom
120 row with those in the top row shows that CCCs obtained using a stronger cutoff approximately mirror
121 those obtained with a weaker cutoff at an earlier time. This behavior implies that CCCs emerge in a
122 highly correlated stochastic process during which cells gradually constrict while maintaining their
123 spatial correlations.
124   Our present study focuses on spatial aspects of the constriction process. Therefore, in the
125 analysis of the constriction patterns *in vivo* we rely on a single MAL reduction cutoff value. We
126 choose $r_c = 0.65$ as the standard cutoff, because for this value the observed correlations between
127 constrictions are most pronounced. Correspondingly, the constrictions in our numerical AGF model
128 (which is described next) are treated as instantaneous. This coarse-graining in time allows us to
129 determine the essential features of the geometry of constriction patterns without considering
130 complexities of temporal aspects of constrictions of individual cells.

131 **The AGF model predicts that tensile-stress feedback between constricting cells results in formation of CCCs**
132
133 Description of the AGF model

Epithelial cell layer represented as a system of interacting particles

To help explain the source of correlations between apical constrictions and the origin and role of CCCs, we will use the AGF model introduced by *Gao et al.* (*2016*). The model treats apical cell ends as mechanically coupled particles and is designed to explore the role of mechanical forces and mechanical feedbacks that occur in the apical surface of the epithelial cell layer.

Unlike more common vertex models (*Farhadifar et al., 2007*; *Hufnagel et al., 2007*), the coarse-grained AGF approach does not describe individual cell membranes but instead the entire apical cell ends are represented as stress-responsive active particles that are capable of random constrictions. Such an approach is chosen because apical constrictions involve not only the actomyosin rings connected to both the cell membrane and the adjacent cells by adherens junctions but also the dynamic stress-bearing actomyosin meshwork in the cortical apex, responsible for ratcheted constrictions (*Martin et al., 2009*). Thus a typical vertex model would be insufficient, and a simpler particle-based AGF model that treats cells as undivided entities described by their effective properties is more adequate.

As depicted in the schematic shown in *Figure 4* and further discussed in the Methods section, the apical cell ends are modeled as mechanically coupled particles interacting via elastic and adhesive forces described using pairwise-additive repulsive and attractive spring potentials,

$$V_r(r_{ij}) = \frac{\epsilon}{2}(1 - r_{ij}/d_{ij})^2 \Theta(d_{ij}/r_{ij} - 1), \tag{2}$$

$$V_a^{np}(r_{ij}) = \frac{\epsilon}{2}(1 - r_{ij}/d_{ij})^2 \Theta(r_{ij}/d_{ij} - 1). \tag{3}$$

Here ϵ is the characteristic energy scale, r_{ij} is the separation between particles i and j, $d_{ij} = \frac{1}{2}(d_i + d_j)$ is their average diameter, $\Theta(x)$ is the Heaviside step function, and the attractive potential V_a^{np} acts only between neighboring particles. The interparticle interaction forces $f_{ij} = -dV_{ij}/dr_{ij}$, where V_{ij} is the sum of the intercellular potentials expressed by *Equation 2* and *Equation 3*, not only give the epithelial layer its mechanical integrity, but also provide feedback that coordinates apical constrictions.

Active, inactive, and constricted particles

The particles in the AGF model are divided into three categories: active particles $\mathcal{A}$ (yellow circles in *Figure 4* and *Figure 5*), inactive particles $\mathcal{I}$ (gray), and particles already constricted $\mathcal{C}$ (black). The active particles occupy a stripe approximately 12 particles wide and 80 particles long, corresponding to the size of the mesoderm primordium in the *Drosophila* embryo (*Sweeton et al., 1991*). These particles undergo a stochastic constriction process in which a particle i can instantaneously constrict by reducing its diameter $d_i \rightarrow f_c d_i$, where $f_c = 0.6$ is the constriction factor. Since we focus on ratcheted cell-constriction events, i.e., constrictions after which a cell does not subsequently expand (*Xie and Martin, 2015*), we assume that already constricted particles do not unconstrict or undergo any other size changes.

The inactive particles $\mathcal{I}$ occupy the region outside the mesoderm primordium. These particles do not exhibit any constriction activity. However, they are an important part of the system, because they provide mechanical environment for the constriction process.

Stress-correlated stochastic constrictions

To describe a stress-correlated stochastic constriction process, we perform a sequence of simulation steps in which each active particle i can constrict with the stress-dependent probability $P_i(s_i)$, where s_i is the feedback parameter associated with tensile forces acting on the particle. The constrictions are followed by mechanical relaxation of the medium to ensure that the process is quasistatic and therefore governed by the equilibrium stress distribution.

In our numerical model, the feedback parameter

$$s_i = (\sigma_i/\sigma_{ref})^p \Theta(\sigma_i) \tag{4}$$
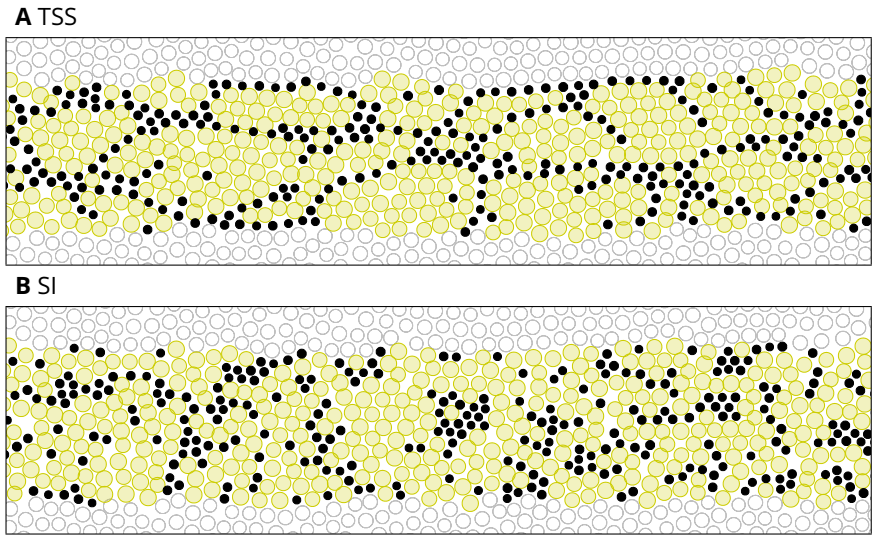
A TSS

B SI

Figure 5. The effect of tensile-stress feedback on the cellular constriction pattern. The figure shows predictions of the AGF model for the multicellular patterns formed by constricted cells for (**A**) tensile stress sensitive (TSS) system and (**B**) stress insensitive (SI) system when 40% of cells in the active region have constricted. The tensile-stress feedback present in A results in formation of chains of constricted particles, similar to the CCCs observed during the initial phase of VFF (see Fig 2).

178   is given in terms of the triggering stress exerted on the particle i by its surrounding cells,

$$\sigma_i = -\epsilon^{-1} \sum_{j \neq i} d_{ij} f_{ij}. \tag{5}$$

179   The Heaviside step function Θ in the feedback parameter defined by **Equation 4** selects the tensile-
180   stress domain $\sigma_i > 0$, and p is the stress-sensitivity profile parameter. As in our previous study (**Gao**
181   **et al., 2016**) we use $p = 3$, which corresponds to enhanced sensitivity to large stresses. The stress
182   σ_i in **Equation 4** is normalized by the average tensile stress σ_{ref} experienced by a single particle
183   constricted in the initial configuration.

184   The constriction probabilities $P_i(s_i)$ are calculated according to the linear relation

$$P_i(s_i) = \frac{\alpha_i(1 + \beta s_i)}{N_a(1 + \beta)}, \tag{6}$$

185   where N_a is the current number of unconstricted active particles, introduced to ensure that approx-
186   imately the same number of particles constrict in each simulation step. The coupling constant $\beta \geq 0$
187   determines the responsiveness of cellular constrictions to the stress feedback parameter s_i, with
188   $\beta = 0$ corresponding to the stress insensitive (SI) case, and $\beta \to \infty$ describing a system where tensile
189   stress is required for constrictions. Throughout this paper we will use $\beta = 10^4$ in our simulations of
190   tensile-stress sensitive (TSS) systems; this value of β corresponds to a strong stress coupling. The
191   parameter $\alpha_i > 0$ determines the overall magnitude of the constriction probability of a given cell. In
192   our simulations, we generally consider $\alpha_i = 1$ (the same value for all cells); however, α_i is different
193   for cells in different regions of mesoderm primordium in our robustness tests.

The effect of mechanical feedback on constriction patterns

195   **Figure 5** presents the key result of the AGF simulations that motivate our investigations of the role
196   of mechanical feedback in the constriction process. The top panel, **Figure 5**A, shows the predicted
197   constriction pattern in a TSS system with a strong stress feedback ($\beta = 10^4$); the bottom panel,
198   **Figure 5**B, depicts a purely random pattern of constrictions generated from SI simulations with no
199   mechanical coupling ($\beta = 0$). The results are shown at the stage where approximately 40% of cells
200   have constricted. At this fraction of constricted cells *in vivo*, the embryo would be completing the
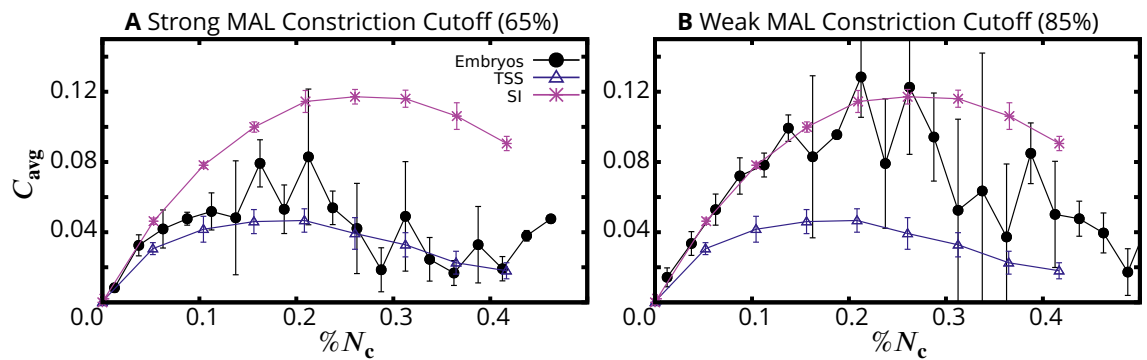201   initial slower phase of VFF (**Sweeton et al., 1991**).

Figure 6. The normalized average number of clusters. Comparison between average total number of clusters C_{avg} for TSS AGF system, SI AGF system, and live embryos. The results are normalized by the number of active cells in each analyzed image or simulation frame (as defined by *Equation 7*). The experimental results are obtained as the average over five embryos, with constricted cells identified using (**A**) a strong MAL reduction cutoff $r_{\mathrm{c}} = 0.65$ and (**B**) a weak reduction cutoff $r_{\mathrm{c}} = 0.85$. Theoretical data are obtained by averaging over ten simulations. The error bars represented the standard deviation. Except for the initial domain $\%N_{\mathrm{c}} < 0.05$, the experimental data for the strong reduction cutoff in panel A closely follow the simulation results for the TSS system.

The simulation frames presented in *Figure 5* indicate that the constricted cells in the TSS system form chains of constricted particles, similar to CCCs observed *in vivo* (see *Figure 2*). In contrast to this morphology, constricted particles in the random SI case form a combination of small clumps and short chains. We note that at the 40% fraction of constricted cells, the chains in the TSS case organize into a percolating network, which is formed by interconnecting shorter chains that are present at the earlier stages of the process.

The physical reason for the formation and growth of CCCs in the TSS system was discussed in our previous study (*Gao et al., 2016*), where it was indicated that chains of constricted cells inherently produce tensile stresses in cells close to the ends of the chain. It follows that particles close to the chain ends are more likely to constrict, which results in chain length increase and stimulates expansion of the chain-like microstructure. We will further discuss CCC formation mechanisms in the sections on the stress field and robustness of VFF.

Size distribution of CCCs observed *in vivo* is consistent with theoretical predictions for a system with tensile-stress feedback

The geometric similarity between the CCCs observed *in vivo* and those predicted by the theoretical AGF model provides strong (though indirect) evidence that mechanical feedback via tensile forces coordinates apical constrictions. To give further corroboration for our conclusion, we now quantitatively compare constriction patterns identified in the *Drosophila* embryo with those generated using the AGF model. To summarize, we show that the analysis of the number and size distribution of constricted cell clusters provides means to differentiate the stress-coordinated constriction process from the uncorrelated one. The results depicted in *Figure 6* and *Figure 7* indicate that the experimental cluster counts are consistent with the theoretical predictions for the TSS constriction model and do not agree with the uncorrelated SI model.

Our theoretical and experimental data for the normalized average number of clusters

$$C_{\mathrm{avg}} = \langle N_{\mathrm{cl}}/N_{\mathrm{a}}^{0} \rangle \tag{7}$$

are plotted in *Figure 6*. Here N_{cl} is the number of constricted-cell clusters observed in a given image or simulation frame, and N_{a}^{0} is the number of active cells (combining the constricted and unconstricted ones in the observed image). The average $\langle \cdots \rangle$ is taken over five embryos (experiments) or ten simulation runs (theory). The normalization by the number of active cells in the observed part of the system allows us to compare experimental results in which only a portion of the ventral-furrow region is imaged with simulations of the entire active domain. The corresponding results for the

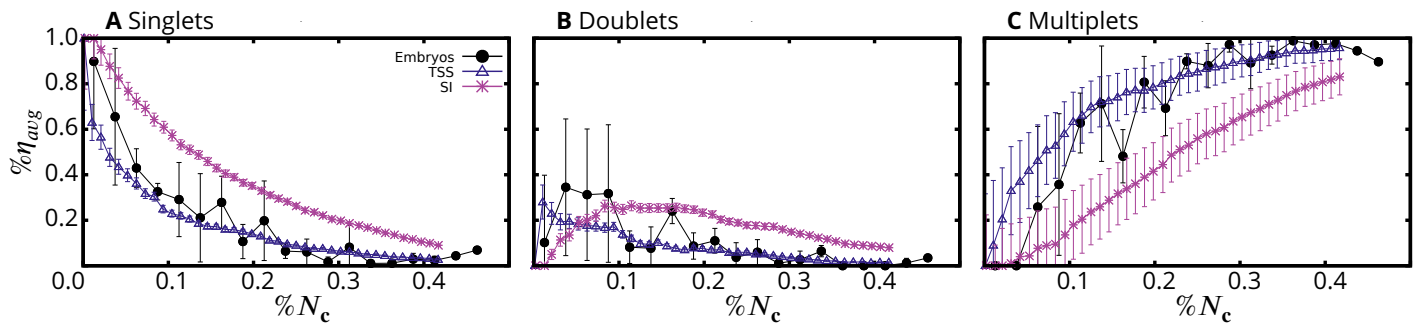Manuscript submitted to eLife

Figure 7. Cluster size distribution. Fraction of constricted particles $\%\eta_{avg}$ in (**A**) singlets, (**B**) doublets, and (**C**) multiplets (3+) for TSS AGF system, SI AGF system, and live embryos. Constricted cells are identified using the standard strong MAL reduction cutoff $r_c = 0.65$. The results are obtained from the same sets of processed embryos and AGF simulations as the ones presented in *Figure 6*. Except for the initial domain $\%N_c < 0.05$, the experimental data closely follow the simulation results for the TSS system.

232 average fraction $\%\eta_{avg}$ of constricted cells in singlets, doublets, and larger clusters are depicted in
233 *Figure 7*.

234 The results illustrated in *Figure 6* and *Figure 7* are plotted vs the fraction of active cells that have
235 constricted, $\%N_c$. The predictions from the AGF model are shown for the SI system (pink stars) and
236 TSS system with $\beta = 10^4$ (purple triangles). The experimental data (black circles) are presented for
237 our standard MAL constriction cutoff $r_c = 0.65$, except for the results shown *Figure 6*B, in which we
238 use a weaker cutoff $r_c = 0.85$ to provide additional insights.

239 Theoretical predictions
240 The morphology depicted in *Figure 5* indicates that the tensile-stress coupling promotes the growth
241 of constriction chains over the creation of new ones. In contrast, there is no such mechanism in the
242 SI system. We thus anticipate that uncorrelated constrictions tend to produce a larger number of
243 smaller clusters, whereas correlations associated with tensile-stress feedback promote a smaller
244 number of larger clusters. The predictions from the AGF model, plotted in *Figure 6* and *Figure 7*,
245 are consistent with the above qualitative analysis.

246 The AGF simulations show that the normalized number of clusters C_{avg} is lower by more than
247 factor of two in the TSS case; the number of singlets is also significantly reduced as compared
248 to the SI system. The behavior of the fraction of particles in doublets is more subtle. In the SI
249 case, the number of doublets increases for $\%N_c \lesssim 0.1$, then flattens out, and gradually decreases.
250 The decay stems from the fact that the doublets are removed from the population by growth into
251 larger clusters due to random constrictions of the neighbors. In the TSS case we observe a similar
252 behavior, but the initial spike and the subsequent decrease of the fraction of doublets are much
253 more pronounced because of the constriction correlations introduced by the stress feedback. The
254 effect of the stress-induced correlations is also seen in the large fraction of particles in multiplets in
255 the TSS case.

256 A comparison between experimental data and the theory
257 We now turn to the distribution of clusters of constricted cells in live embryos. We focus on clusters
258 identified using the benchmark MAL reduction cutoff value $r_c = 0.65$. Our principal observation is
259 that the experimental data (depicted in *Figure 6*A and *Figure 7* by black circles) are consistent with
260 the theoretical predictions for the TSS system but not with those for the uncorrelated SI system.

261 This clear trend is consistently seen for all quantities considered, i.e., for the normalized number
262 of clusters (*Figure 6*A) and the distribution of singlets, doublets, and multiplets (*Figure 7*). We find
263 that the experimental results agree, within the statistical inaccuracies, with the theoretical results
264 for the TSS system. Moreover, the experimental data consistently differ from the results for the SI
265 system considerably more than by the standard deviation represented by error bars.

266 The essential qualitative features of the cluster distribution predicted theoretically for the tensile-

stress correlated constrictions are markedly present in the experimental curves. In particular, the fraction of singlets quickly decays when the constriction process progresses; the initial rapid growth of the population of doublets is followed by a decrease to nearly zero; and a large fraction of constricted cells form multiplets. Thus our results not only show that apical constrictions are spatially correlated but also provide evidence that these correlations are a consequence of mechanical feedback via tensile stress.

While the overall agreement between the theory and experiments is quite compelling, there is a discernible discrepancy at the beginning of the constriction process. Namely, for the constricted-cell fractions $\%N_c$ below approximately 0.05, the experimental results show noticeable overpopulation of singlets and underpopulation of multiplets as compared to theoretical predictions for the TSS system. Moreover, we observe that in this initial CCC formation regime the experimental results follow the curves for the uncorrelated SI constriction process.

The likely source of this initial uncorrelated behavior is a delay in cell response to mechanical feedback *in vivo*. Because of this delay, spatial correlations between apical constrictions need some time to build up. Such a delay is not built in into our coarse-grained AGF model because we want to keep the model simple without introducing unnecessary fitting parameters.

Furthermore, our experimental results show that the delay of establishing a spatially correlated constriction pattern is much more pronounced for weaker constrictions. This phenomenon can be seen in the results presented in *Figure 6*B for the normalized number of clusters of constricted cells identified using the MAL reduction cutoff $r_c = 0.85$. The results obtained using this weak cutoff correspond mostly to pulsed unratcheted constrictions. We find that the experimental data follow the random SI result until approximately 25% cells constrict. Subsequently, the measured number of clusters crosses over towards the theoretical curve for the TSS system. This long delay before the correlations between weak constrictions are established likely stems from the fact the small-amplitude constrictions produce weak stresses. A significant feedback occurs only after the stress builds up when the number of constricted cells and/or constriction amplitude become sufficiently large.

The results obtained using strong and weak MAL thresholds, taken together present a cohesive picture of the initial slow phase of apical constrictions. Cells begin pulsing stochastically, generating fleeting bursts of tensile stress through the mesoderm primoridum. These stress bursts combine constructively to trigger some cells to begin ratcheted apical constrictions. Cells performing ratcheted apical constrictions generate a consistent underlying stress field that permeates the mesoderm primoridum, promoting the triggering of ratcheted apical constrictions along paths of high tensile stresses.

CCCs Develop Along Underlying Chains of Aligned Tensile Stress

Important insights regarding the growth of CCCs can be gained from an analysis of the underlying stress distribution predicted by the AGF model. Our discussion will focus on the dynamics of the TSS system, with the uncorrelated SI system being used as a basis for comparison. In the time lapse simulation frames shown in *Figure 8*, the stress is characterized in terms of the major principal stress and the direction of its axis. The stress tensor is evaluated from the virial expression (see *Equation 10*), as discussed in the Methods section.

We use here the following color coding and notational convention: inactive cells are outlined in grey, active cells in orange, and constricted cells in black with a black dot in the center. The fill color of both active and constricted cells indicates whether the cell is under tension (red) or compression (blue); deeper color saturation corresponds to stronger major stress magnitude. Active and constricted cells experiencing an above average stress magnitude are also tagged with a black bar showing the orientation of the major stress axis on each particular cell.

An examination of the sequence of TSS time lapse frames depicted in *Figure 8*A shows that formation of CCCs is a highly nonlocal process. It involves not only tensile stresses in the immediate neighborhood of already constricted cells, but also relies on the nonuniform stress distribution
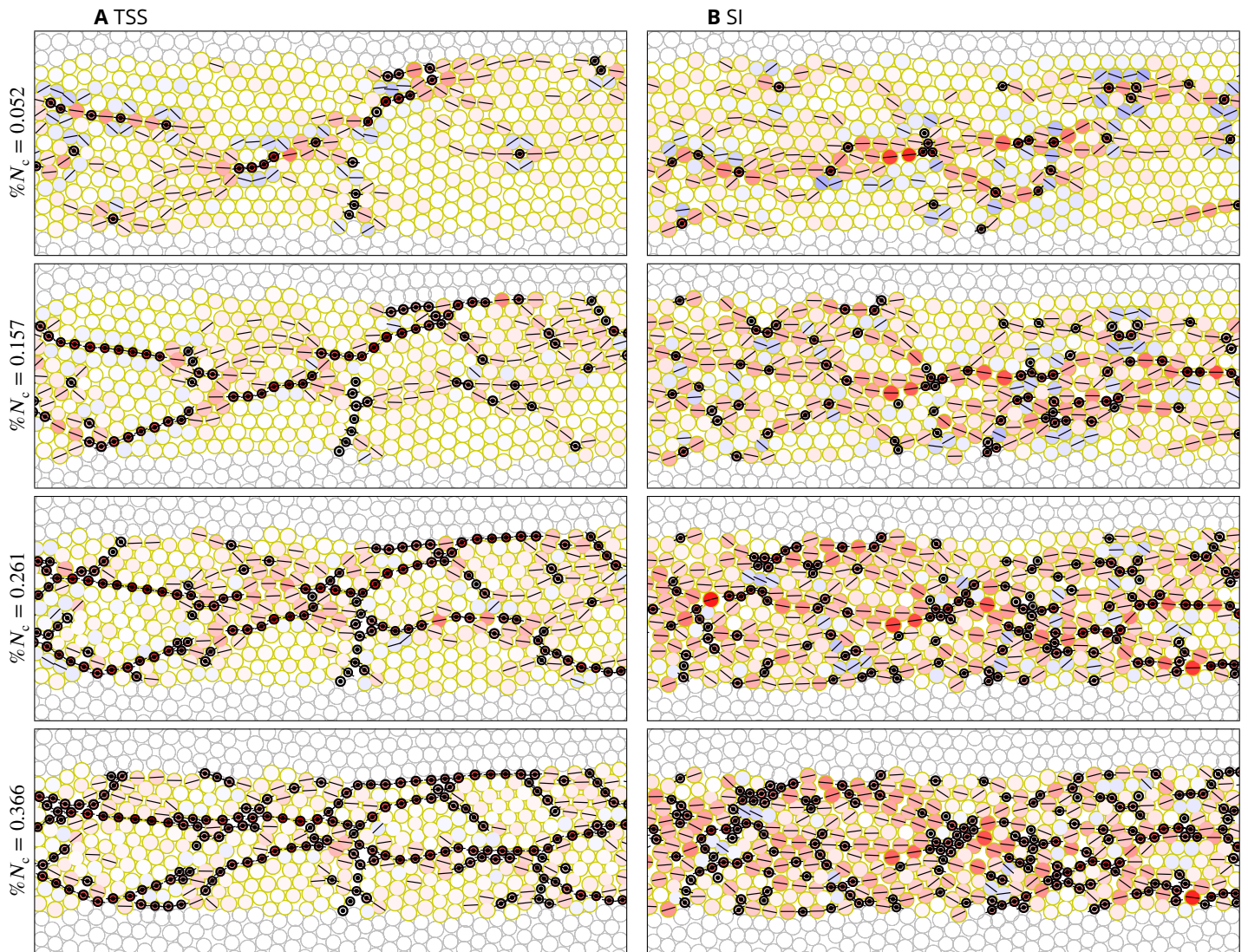
Figure 8. Development of the stress field in the active region. Time lapse AGF simulation frames of a (**A**) tensile stress sensitive (TSS) and (**B**) stress insensitive (SI) system colored to show the distribution of major stresses through the active region. Inactive cells are outlined in gray and active cells in orange; constricted cells are outlined in black and are marked with a dot in the center. The fill color of all active and constricted cells shows tensile (red) and compressive (blue) major stresses, where the color saturation indicates relative strength. Black lines in the direction of the major-stress axis are drawn for cells with the major stress stronger than the average during each snapshot. Linear arrangements of red particles with aligned major stress axis indicate that in both TSS and SI systems the stress propagates along stress chains. In the TSS system these chains are precursors of CCCs, which eventually carry most of the tensile stress in the active region.
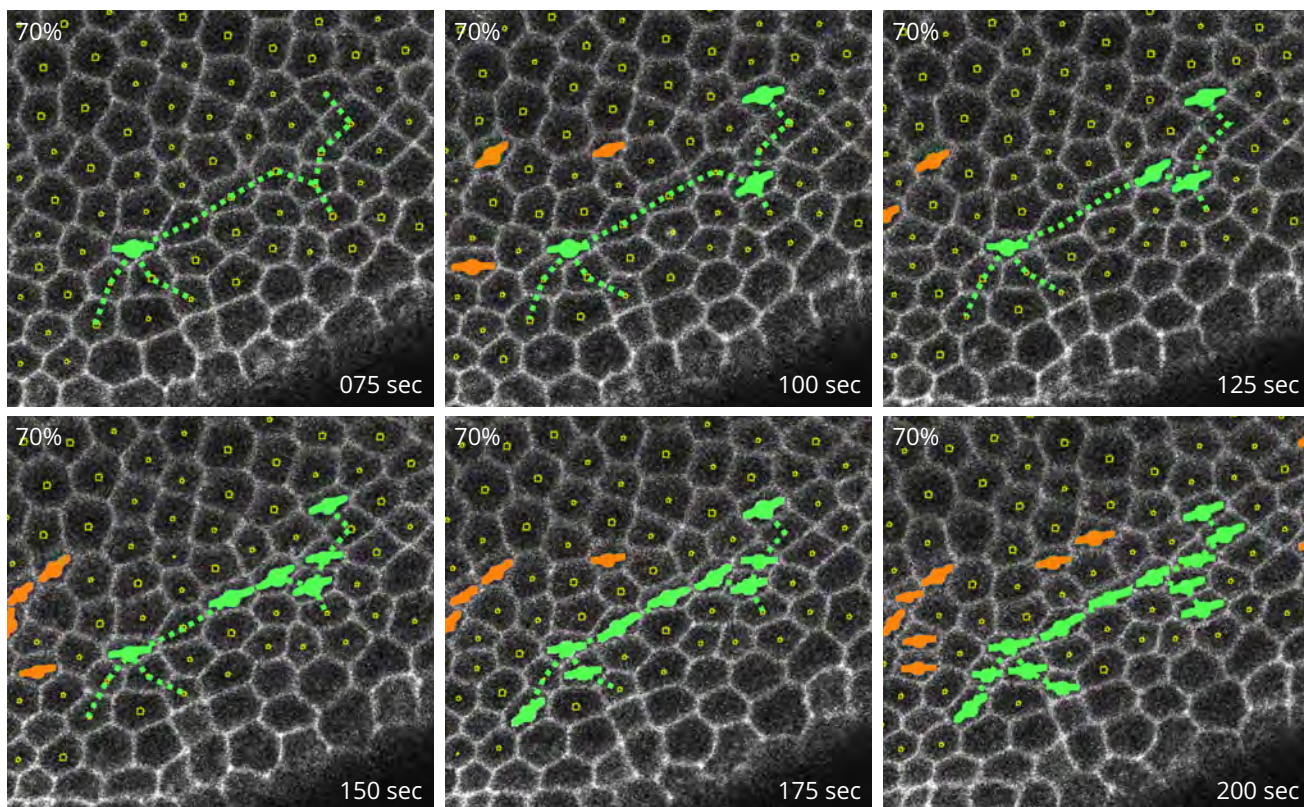
Figure 9. Piecewise formation of a CCC. Processed confocal microscopy images of the ventral side of a Spider-GFP embryo during the initial slow apical constriction phase of ventral furrow formation (VFF). Constricted cells are identified using $r_c = 0.70$; time zero is selected as the first frame with the standard $r_c = 0.65$ that has a constricted cell that persists across multiple frames. The constricted cells highlighted in green initially form linearly arranged singlets and doublets, which are later connected into a single CCC. As an eye guidance, the dotted line indicates the final connectivity of the CCC.

317 associated with the formation of tensile stress chains, defined as groups of linearly arranged
318 particles with above-average tension aligned in the chain direction. In *Figure 8* the stress chains
319 are visible as linear groups of red particles (the color indicating high tensile stress) with aligned
320 black bars indicating the major stress axis. The stress chains we observe in the AGF system are
321 closely related to force chains along which stress propagates in granular media (*Kondic et al., 2012*;
322 *Tordesillas et al., 2015*).

323 The progression of the constriction process depicted in the subsequent frames of *Figure 8*A
324 indicates that the stress chains are precursors of CCCs. Consider, for example, the behavior of
325 the line of cells seen in the top–right of the active region. These cells are under tension (red) for
326 $\%N_c = 0.052$, and by $\%N_c = 0.261$ most them have constricted. In many instances the CCCs in the
327 TSS system do not emerge by adding cells one by one to an already existing chain. Instead of such a
328 continuous-growth progression, the constricted particles initially form singlets and doublets along
329 the stress chain, to be later connected into a larger chain through constrictions of the missing cells
330 in the CCC.

331 The above behavior is evident in the stress chain seen at the top–left of the active region in
332 *Figure 8*A. This stress chain has three singlets and a doublet embedded in it at $\%N_c = 0.052$, and
333 becomes a single CCC at $\%N_c = 0.157$. Similar initially disconnected chains develop *in vivo*, as shown
334 in a representative image in *Figure 9*. Such piecewise formation of CCCs provides further evidence
335 that tensile-stress feedback coordinates apical constrictions.

336 The stress chains are mostly arranged in the longitudinal direction because the inactive lateral
337 regions provide only a moderate mechanical resistance. Thus, the CCCs emerging as a result of
338 mechanical feedback are also mostly oriented longitudinally. This feature is consistent with the
339 experimental observations showing chains of constricted cells oriented primarily in the anteropos-
340 terior direction.

AGF model predicts that tensile-stress feedback aids robustness of VFF

342 In this and the following section we address the question of how the embryo can achieve robustness
343 of VVF in the presence of spatial fluctuations of cell ability to constrict. In live embryos such
344 fluctuations can occur naturally due to randomness of biophysical processes. Local fluctuations can
345 also be produced experimentally, using optogenetic techniques (*Guglielmi et al., 2015*).

346 To generate theoretical predictions for possible effects of mechanical feedback on robustness of
347 VFF, we consider an AGF model system with locally reduced magnitude of the constriction probability
348 function. The reduction is achieved by decreasing the probability amplitude α_i (see *Equation 6*) for
349 active particles in a prescribed disrupted region. *Figure 10* and *Figure 11* show results for a band
350 of affected active cells, and in *Figure 12* the disrupted region is in a shape of an ellipse. In both
351 cases we find that tensile-stress feedback introduces mechanisms for robustness of the constriction
352 process.

353 In this section we use the following color coding convention. Inactive cells are outlined in grey,
354 active unaffected cells in orange, active perturbed cells in green, and constricted cells in black with
355 a black dot in the center. The fill color will follow the same color and saturation convention as the
356 one used in *Figure 8*, with tensile major stresses being red and compressive being blue. Active
357 or constricted cells experiencing an above average stress magnitude will again have a black bar
358 representing the orientation of the majors stress.

359 Affected band model

360 *Figure 10* shows particle configurations and stress distributions for systems with a band of cells
361 whose constriction probability amplitude (the factor α_i in *Equation 6*) has been decreased by by 40%
362 (top), 60% (middle), and 80% (bottom) as compared to the reference value $\alpha_i = 1$ for the unaffected
363 active cells. Simulation frames are presented for the fraction of constricted cells $\%N_c = 0.3$; the
364 affected particles are in the green region between two vertical lines, and the unaffected particles
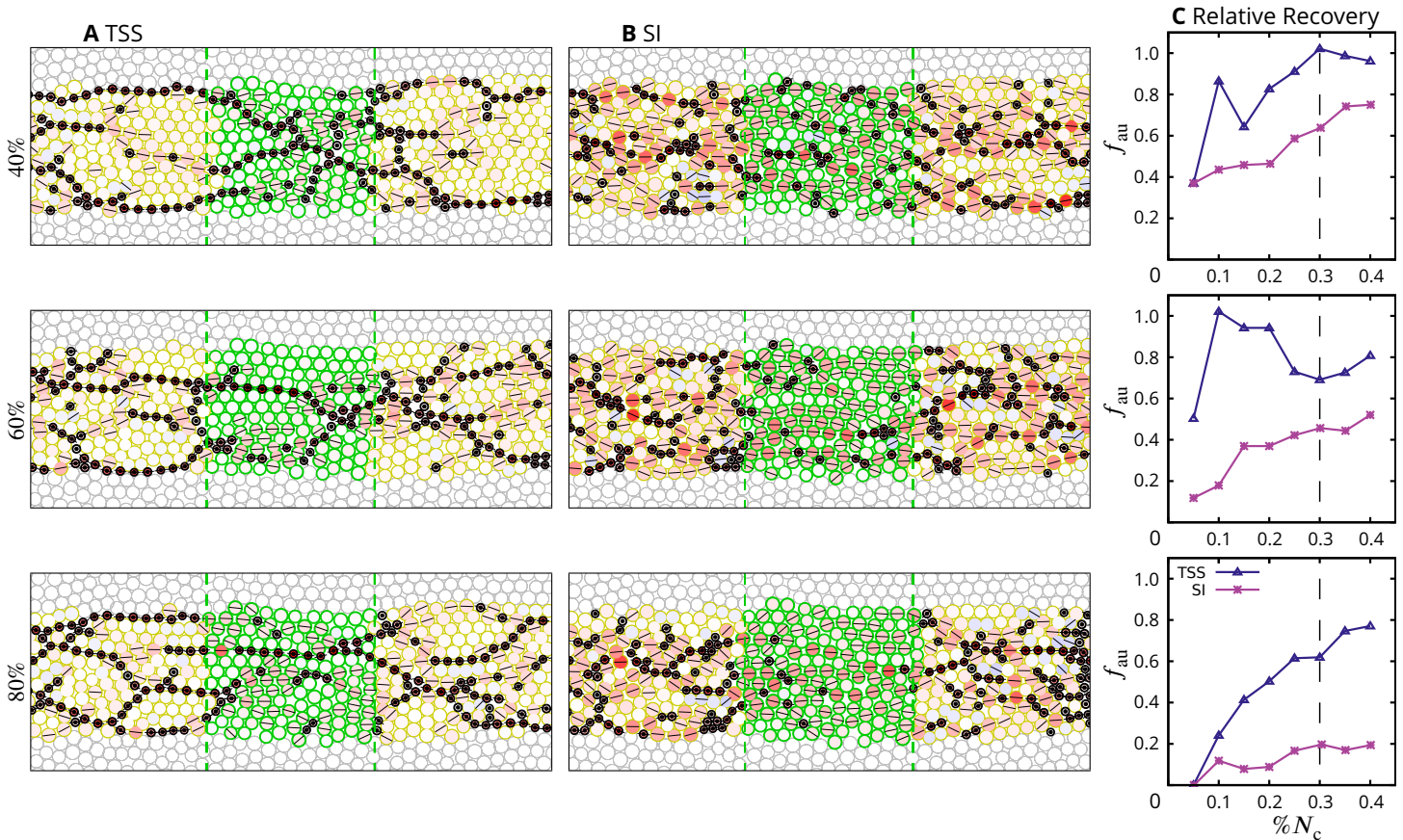
Figure 10. AGF system with a band of cells of decreased constriction probability. Simulation snapshots for a (**A**) tensile stress sensitive (TSS) and (**B**) stress insensitive (SI) system with a band of cells whose constriction probability is reduced by 40%, 60%, and 80%. The images follow the color convention used in *Figure 8*, with the addition of cells outlined in green to represent active cells with the reduced constriction probability in the affected area between the two dashed lines. (**C**) Plots showing the constriction-reduction factor f_{au} vs the fraction of constricted cells $\%N_c$ for systems for which representative simulation frames are depicted in A,B. The frames correspond to $\%N_c = 0.3$, which value is indicated by the dashed black lines in C. The constriction-reduction factor f_{au} (defined in *Equation 8*) reflects how well the affected region is performing compared to the unaffected areas, with $f_{au} = 1$ indicating full recovery of the affected region. All three plots show that TSS system exhibits substantial recovery at sufficiently large values of $\%N_c$. This behavior provides evidence that tensile stress feedback enhances robustness of the constriction process.

365 in the orange regions. The results are depicted for both TSS and SI constrictions to highlight the
366 differences in the system development with and without the stress feedback.

367 We start our discussion with the observation that the constriction patterns and stress distribu-
368 tion in the unaffected regions are similar to those in a uniform system with a similar fraction of
369 constricted cells (see the results depicted in *Figure 8* and *Figure 10*). We thus focus our analysis on
370 the disrupted regions, i.e., the regions with the reduced constriction probability amplitude $\alpha_i < 1$.

371 The examination of the affected regions between the two vertical lines in *Figure 10*A and
372 *Figure 10*B shows a striking difference between the uncorrelated SI system and the TSS system
373 with mechanical feedback. In the purely random SI case the fraction of constricted cells in the
374 affected band is reduced by a factor that is commensurate with the imposed decrease in the
375 constriction probability. For example, in the SI system with 80% reduction there are only a few
376 constricted particles in the affected domain. In contrast, in the corresponding TSS system there
377 is a CCC percolating through the affected band, and the overall number of affected particles that
378 have constricted is much larger. A similar behavior is observed at lower values of the probability
379 amplitude reduction. In particular, in the TSS system with a moderate 40% reduction of the
380 probability amplitude α_i, the only distinguishable feature of the disrupted region is an additional
381 buildup of tensile stresses there, as compared with the unaffected regions.

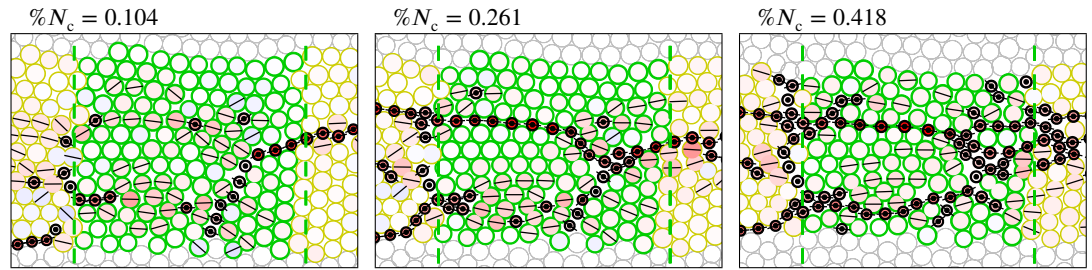382 To quantitatively compare the affected band of cells to the unaffected regions we consider the

Manuscript submitted to eLife

$\%N_c = 0.104$ $\%N_c = 0.261$ $\%N_c = 0.418$

Figure 11. Rescue mechanism for cellular constrictions via tensile-stress feedback. Blow-up view of the band of affected particles in a TSS system with the constriction probability in the affected region reduced by 60%. The images follow the color convention used in *Figure 10*. The left frame of the time-lapse sequence shows the initial formation of tensile-stress chains crossing the affected zone. The constriction probability is elevated along these chains because of tensile-stress feedback. Thus particles constrict along the precursor stress chains, forming CCCs crossing the affected region.

383 constriction-reduction factor

$$f_{au} = \frac{\%N_c^a}{\%N_c^u}, \tag{8}$$

384 where $\%N_c^a$ and $\%N_c^u$ denote the fraction of active cells that constricted in the affected and unaf-
385 fected regions, respectively. According to the above definition, $f_{au} = 1$ occurs if the affected region
386 recovers to the normal behavior.

387 The constriction-reduction factor f_{au} is shown in *Figure 10*C vs the fraction of constricted cells
388 $\%N_c$ for the systems depicted in *Figure 10*A and *Figure 10*B. We find that f_{au} is consistently higher
389 for TSS constrictions (purple triangles) than the corresponding quantity for SI constrictions (pink
390 stars). Moreover, due to the presence of tensile feedback, the constriction-reduction factor f_{au} in
391 the TSS case is close to one at $\%N_c = 0.4$, even for the 80% probability reduction. This result implies
392 that tensile-stress feedback produces nearly full constriction recovery at the development stage
393 corresponding to the onset of the fast VFF phase *in vivo*.

394 The rescue mechanism

395 The mechanism by which tensile-stress feedback rescues apical constrictions in the disrupted zone
396 is illustrated in *Figure 11*. The left panel shows that constrictions, which initially occur with higher
397 frequency in the unaffected domain, cause gradual buildup of tensile stress chains in the affected
398 region. Thus, due to the mechanical feedback represented in *Equation 6* by the parameter s_i, the
399 constriction probability is elevated for the affected cells under tension.

400 Hence, CCCs penetrate the affected zone along the tensile stress chain, as depicted in the
401 right panel of *Figure 11*, rescuing the constriction process. The above analysis clearly indicates
402 that the mechanical feedback may offer robustness of VFF by providing a mechanism to even out
403 irregularities of the pattern of constrictions. Since the constricted cells carry most of the tensile
404 stress, consistent constriction pattern along the furrow facilitates coherent invagination.

405 Elliptical Affected Region

406 *Figure 12* shows the progress of apical constrictions in a TSS system with an ellipsoidal affected
407 region at the center of the active domain. The lateral size of the ellipse is of about 75% of the
408 width of the active region, so there are unaffected cells above and below the ellipse. The time-
409 lapse images are presented for a moderate 40% and complete 100% reduction of the constriction
410 probability.

411 The depicted simulation frames indicate that CCCs promote recovery of a balanced constriction
412 pattern in two ways, depending on how strongly the affected region is perturbed. At the moderate
413 probability reduction, the prevailing recovery mechanism is the penetration of CCCs into the affected
414 region after the stress chains build up. This mechanism is the same as the one described for a band
415 of affected cells. For the 100% constriction probability reduction (α_i reduced to zero) the affected
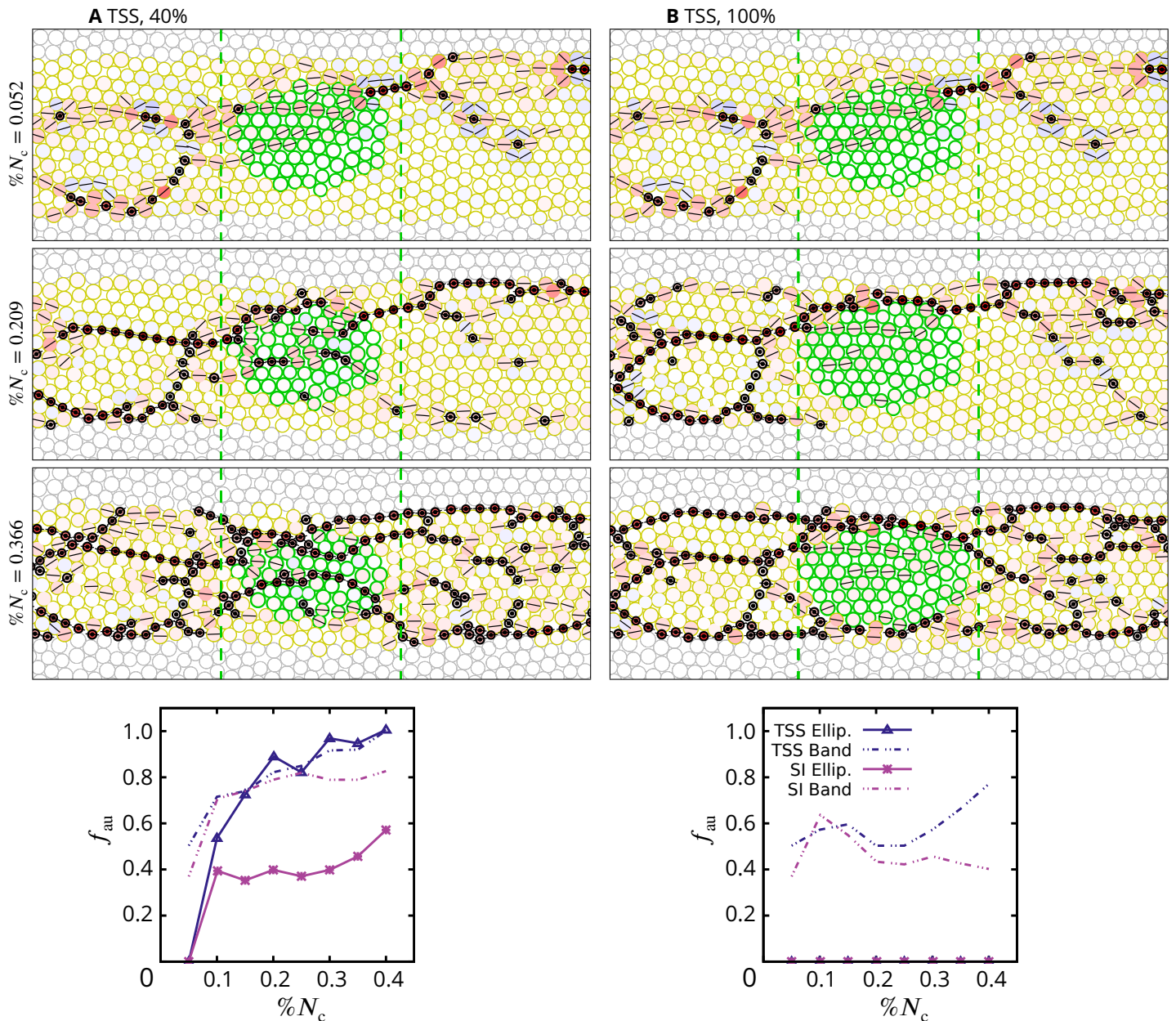
Figure 12. AGF system with an elliptical region of decreased constriction probability. Time-lapse simulation frames and corresponding graphs of the constriction-reduction factors for a TSS system with an elliptic region of cells whose constriction probability is decreased by (**A**) 40% and (**B**) 100%. The images follow the color convention used in *Figure 8*, with the addition of cells outlined in green to represent active cells with the reduced constriction probability in the affected area between the two dashed lines. The graphs show two different measures of recovery: the constriction-reduction factor f_{au} for the affected elliptical region and the corresponding factor $\bar{f}_{au}$ for the band of cells that includes the affected region and the active cells below and above it (i.e., the entire area between the dashed green vertical lines). The constriction-reduction factors are plotted both for the simulations shown in the depicted frames and for the corresponding SI system with no feedback. For 40% reduction of the probability, A, the TSS system undergoes constriction recovery by penetration of CCCs into the affected ellipsoidal region; for 100% reduction, B, the recovery occurs by CCCs wrapping around the affected ellipse.

416 cells cannot constrict. In this case we observe that CCCs wrap around the affected ellipse instead of
417 penetrating it. In spite of severity of the local constriction disruption, formation of the envelope of
418 CCCs around the affected region results in a relatively uniform constriction pattern.
419   To quantitatively characterize the chain-penetration and wrapping-around mechanisms by which
420 mechanical feedback rescues a balanced constriction pattern we consider two complementary
421 measures of recovery (see the graphs on the bottom of *Figure 12*). The first measure is the relative
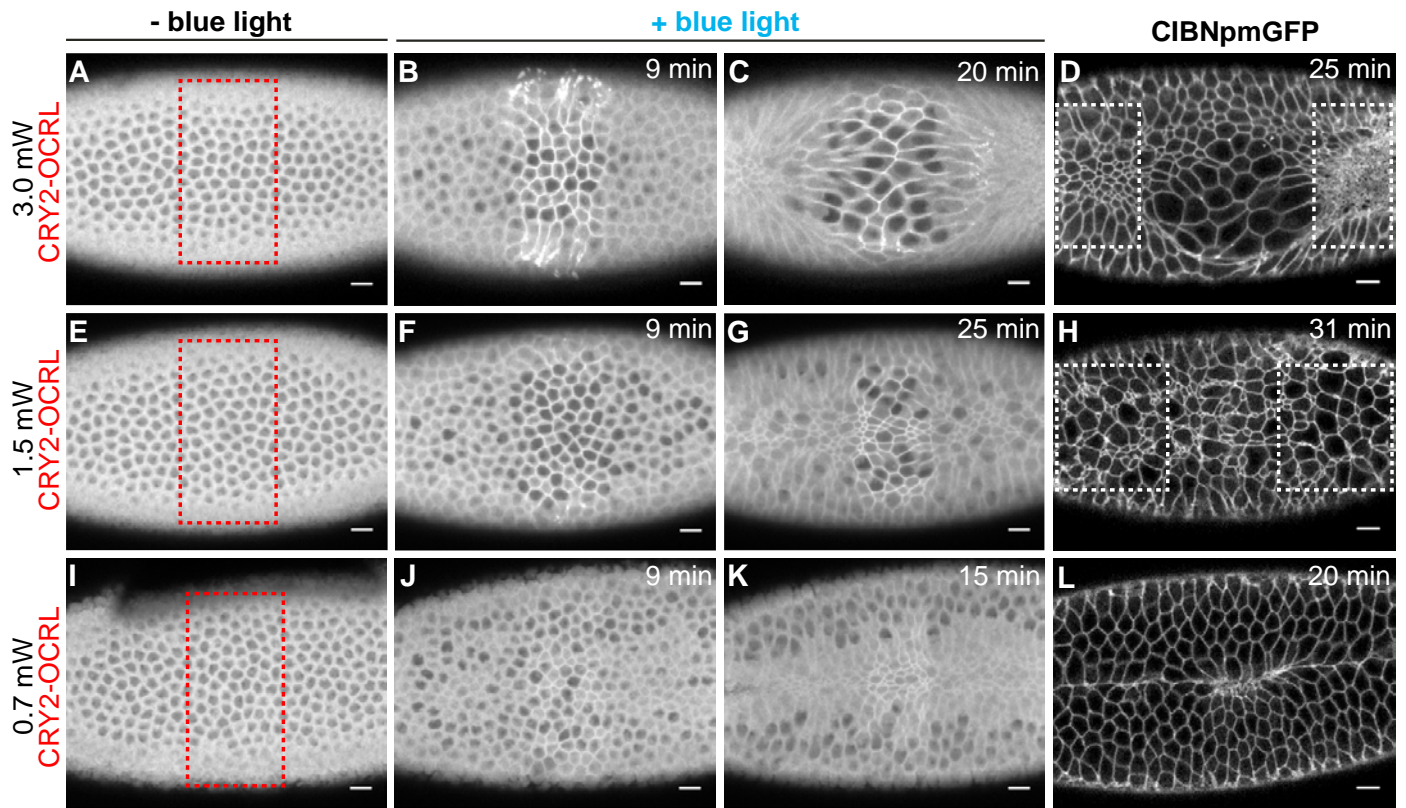
Figure 13. Confocal images of representative embryos with a zone of optogenetically reduced contractility. The images show the apical surface of the ventral mesoderm of optogenetically engineered embryos. To locally reduce cell contractility, the embryos were exposed to blue light in the zone indicated by the red box in left panels. The power of blue light is proportional to the amount of cell contractility reduction. The affected zone was photo activated with (**A**)–(**D**) 3 mW, (**E**)–(**H**) 1.5 mW, and (**I**)–(**L**) 0.7 mW laser beam. The first three images in each row are still images from a confocal movie, and the last frame is a high-resolution confocal image. Time after photo-activation as indicated. For 0.7 mW and 1.5 mW laser power, the images show a significant number of constricted cells in the affected region, forming chain-like arrangements. For the 3.0 mW laser power, constricted cells appear to wrap around a large cluster of unconstricted (expanded) cells. Figure reprinted from *Guglielmi et al.* (*2015*) under the article's CC BY license.

422   fraction of constricted cells in the affected region f_{au}, as defined by *Equation 8*. This quantity
423   characterizes constriction rescue by the penetration of CCCs into the affected region. The second
424   measure is the relative fraction of constricted cells evaluated for the entire band of active cells that
425   encompasses the affected region (see the area between the two dashed green lines in time lapse
426   images of *Figure 12*). This measure (denoted $\bar{f}_{au}$) includes contributions from both the penetrating
427   and wrap-around chains.

428   The results depicted in the graph shown at the bottom of *Figure 12*A indicate that for a moderate
429   probability-amplitude reduction, the fraction of constricted cells in the affected region is completely
430   recovered before the system reaches the fast-phase threshold $\%N_c = 0.4$. The recovery is manifested
431   in both measures f_{au} and $\bar{f}_{au}$. In the case of the probability reduction to zero we have $f_{au} = 0$, because
432   there are no constrictions in the affected region. However, the parameter $\bar{f}_{au}$ shows that there is a
433   significant recovery of the constriction pattern by the wrap-around mechanism.

434   **Optogenetic experiments provide evidence of robustness of apical constrictions in**
435   **Live Embryos**
436   Optogenetic inhibition of cell contractility in experiments by *Guglielmi et al.* (*2015*)
437   The results of our computational investigations of the TSS systems with locally lowered constriction
438   probability are strikingly similar to experimental findings by *Guglielmi et al.* (*2015*). These authors
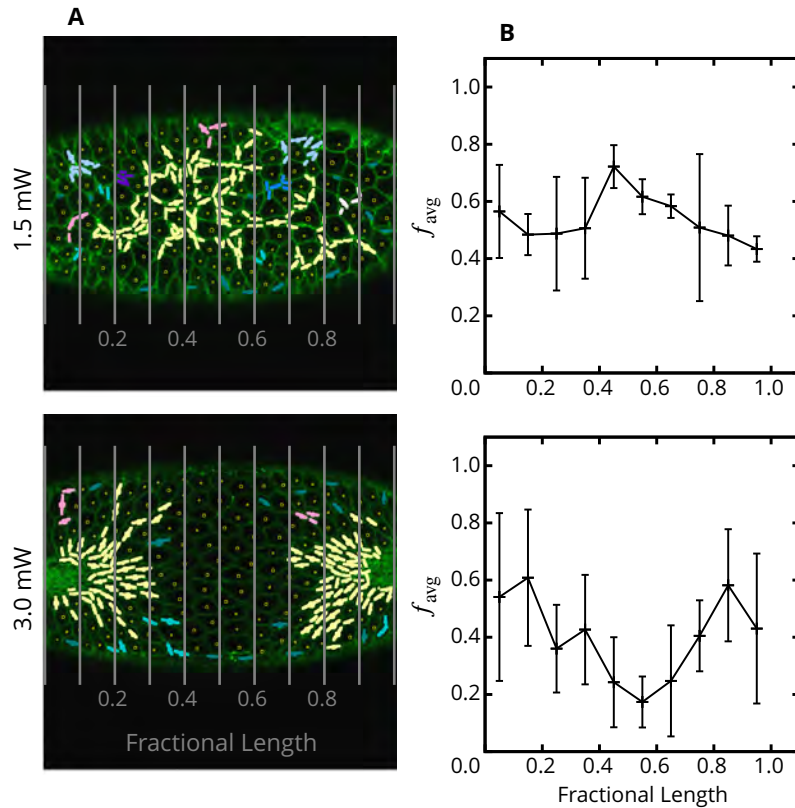
Figure 14. Processed images and calculated fractions of constricted cells in optogenetically disrupted embryos. (**A**) Representative images of embryos which failed to complete VFF due to having a band of cells about their length center optogenetically activated with 1.5 mW (top) and 3.0 mW (bottom) laser. The cells have been marked as constricted if their MAL is below the cutoff value of 1.3 μm. (We do not use relative MAL reduction as the constriction criterion because of unavailability of the reference data). The colors represent the number of cells belonging to a single constricted-cell cluster according to the scale defined in *Figure 2*. Notice that CCCs penetrate the affected region for the 1.5 mW case but not the 3.0 mW case. (**B**) Averaged binned fraction of constricted cells, f_{avg}, vs fractional position along the observed portion of the mesoderm primordium, as defined by the vertical lines in the corresponding images shown in A. (Averages over $n = 3$ embryos.) The results for 1.5 mW laser beam do not show any constriction deficit in the affected region, indicating a recovery of contractile activity, consistent with our predictions. For 3.0 mW laser power there is a significant deficit of constrictions in the affected zone, but the contractile activity does not drop to zero.

439 developed an optogenetic approach to locally affect the ability of cells to contract during VFF in the
440 *Drosophila* embryo. Specifically, they targeted PI(4,5)P2 to rapidly deplete actin from the embryonic
441 cell cortex and therefore to reduce actomyosin contractility in a photo-activated region.

442 As depicted in *Figure 13*, reprinted from their study, *Guglielmi et al.* (*2015*) used three different
443 levels of laser power to optogenetically modulate the contractility in a band of cells in the central
444 part of mesoderm primordium. The photo-activated band is analogous to the affected zone in
445 our AGF model; we will thus discuss their experimental results in the context of our theoretical
446 predictions.

447 Illuminating the embryo using different laser powers allowed *Guglielmi et al.* (*2015*) to vary the
448 degree of the local cell contractility inhibition, thus affecting the morphology of the developing
449 tissue to a varying degree. According to *Figure 13*I–L, applying the lowest power level of 0.7 mW
450 did not prevent the ventral-furrow invagination, although there is a clear defect in the furrow
451 morphology seen in *Figure 13*L. For higher levels of the laser power 1.5 mW (*Figure 13*E–H) and
452 3.0 mW (*Figure 13*A–D) there was no transition to the fast phase of VFF and the embryo failed to
453 invaginate.

454 An analysis of constriction patterns at different photo-activation levels

Weak photo-activation

The images shown in *Figure 13*J and K for the lowest level of the optogenetic activation (0.7 mW laser power) reveal constriction chains crossing the affected region of reduced cell contractility (in the middle part of the frame). While the contrast of the images is insufficient for a quantitative comparison, the fraction of constricted cells in the unaffected and optogenetically affected regions appear to be approximately the same, consistent with our theoretical predictions for the rescue of the constriction process in the TSS system.

Moderate photo activation

A similar conclusion can be drawn from an analysis of the images of the embryo illuminated with a moderate power 1.5 mW laser beam. In addition to a visual inspection, we performed a quantitative analysis of experimental data in this case, using high-contrast images that are available for the final state of the constriction process (see the example shown in *Figure 13*H).

An examination of unprocessed images shown in *Figure 13*G and H as well as an analysis of the processed image depicted in the top panel of *Figure 14*A indicate that CCCs penetrate the affected region. This conclusion is quantitatively supported by the corresponding plot of the local fraction of constricted cells presented in *Figure 14*B. The results do not show any deficit of constricted cells in the affected domain, in spite of a significant disruption of the ability of cells to constrict. We recall that our simulations depicted in *Figure 10* predict a substantial recovery of constrictions even at 80% reduction of the constriction probability; thus a strong recovery of the fraction of constricted cells can be expected.

The relatively consistent behavior across 1.5 mW embryos (i.e. affected and unaffected regions behaving similarly) was recognized by *Guglielmi et al.* (*2015*) and attributed to the fact that some cells within the affected area retained the capability to contract while others did not. We provide here a specific interpretation of this behavior in terms of mechanical feedback, which rescues the ability to constrict in cells that are subject to elevated tensile stress.

We also note that, according to *Figure 14*B, the fraction of constricted cells, f_{avg}, in the analyzed frames is larger than 40%. This is because the transition to the second fast phase of VFF has not occurred, and apical constrictions continued beyond the usual 40% slow-to-fast-phase transition threshold. Progression of the slow phase of constrictions beyond the time at which invagination usually takes place (compare the results for 0.7 mW and 1.5 mW power in *Figure 14*) is likely to be responsible for strong bidispersity of cell sizes seen in *Figure 13*H. Namely, the cells in already formed CCCs continued to constrict, causing the others to expand. A similar behavior can be seen in images of embryos with delayed or failed VFF due to injection of Rho kinase inhibitor (*Krajcovic and Minden, 2012*).

Strong photo activation

We now discuss constriction patterns at the highest illumination level. The results depicted in *Figure 13*A–D show that the 3.0 mW laser beam hinders constrictions in the affected zone almost entirely. The optogenetic disruption leaves the cells unable to perform active mechanical responses, and as a result, they stretch and enlarge when being pulled. However, as already noted by *Guglielmi et al.* (*2015*), the cells bordering the affected region still constrict; this behavior is similar to the constriction pattern seen in our simulations for the ellipsoidal affected domain, where tensile-stress sensitivity results in formation of CCCs wrapping around the region of hindered contraction probability (see *Figure 12*B). Consistent with the above observations, the plot shown at the bottom of *Figure 14*B suggests that even at 3.0 mW illumination there is some constriction recovery (although much weaker than in the ellipsoidal-affected-region case in our AGF model).

To summarize our findings, the results of the optogenetic experiments by *Guglielmi et al.* (*2015*) agree well with predictions our theoretical analysis of the role of mechanical feedback in coordinating apical constrictions to enhance robustness of VFF. In particular, the experiments show that chains of constricted cells either penetrate or wrap around the affected region, depending on

the degree of hindrance of cell contractility. Also there is a substantial recovery of constrictions in the optogenetically affected band of cells. These phenomena, predicted by our AGF model, would be difficult to explain without the the assumption that the tensile-stress feedback coordinates cell constrictions.

Discussion

In the formation of the Drosophila ventral furrow (VF), a field of cells, specified by the dorsoventral patterning system to be the mesoderm primordium (*Leptin, 1999*), initiate a multi-step morphological change by flattening their apices (*Leptin and Grunewald, 1990*; *Sweeton et al., 1991*) . The apical actomyosin cytoskeleton undergoes contractile pulses of three varieties: unconstricting, unratchetted constricting and ratchetted constricting pulses (*Martin et al., 2009*; *Xie and Martin, 2015*) . The ratchetted pulses result in progressive apical constriction of particular VF primordial cells (*Xie and Martin, 2015*). Originally thought to be stochastic in nature (*Sweeton et al., 1991*), it was later found that these constrictions were not stochastic and that a cell that had undergone ratchetted apical constrictions, and its neighbors, were more likely to undergo ratchetted constrictions than non-neighboring cells(*Xie and Martin, 2015*).

Our recent work showed that non-stochastic apical constrictions occur at a higher order of organization than neighboring cells. We observed that apical constrictions appeared to form a roughly linear pattern oriented along the anterior-posterior axis shortly before the transition to the fast phase of apical constrictions regulated by Fog and T48 signaling pathways occurred (*Gao et al., 2016*). Apically constricted cells form in chains (CCCs) that extend along the length of the VF primordium. Instead of direct chaining by neighbor to neighbor interactions, our initial observations and modeling results suggested that anterior-posterior-biased chaining occurs along lines of tensile stress with apical constrictions occurring along the chain (*Gao et al., 2016*). Evidence of tensile stress along the anterior-posterior axis of the VF primordium was shown using laser cutting experiments (*Martin et al., 2010*), and was supported by our earlier modeling efforts (*Gao et al., 2016*).

Here, we extend the preliminary observations and results in a statistical comparison between our active granular fluid (AGF) model and detailed confocal imaging of live embryos undergoing ratchetted apical constrictions. The key observations of our theoretical and experimental investigations include:

1. A quantitative agreement between the measured distribution of clusters of constricted cells *in vivo* and theoretical predictions for a system with tensile stress sensitivity.
2. Theoretical establishment that CCCs form along a scaffolding of underlying paths of aligned tensile stress and predominantly grow along the anterior-posterior axis due to anisotropic mechanical stresses.
3. Temporal development of CCCs often occurs through the formation of disconnected smaller clusters, lying along the same path of aligned tensile stress, that are later connected into a single larger chain.
4. Theoretical results showing that tensile stress sensitivity introduces two robustness mechanisms: recovery of cells with reduced contractility through triggering by mechanical stress feedback and redirection of the path of underlying stress to allow CCCs to circumvent regions of impaired contractility. These theoretical results are supported by our analysis of experimental perturbations conducted by *Guglielmi et al.* (*2015*).

We find that the pattern of ratchetted apical constrictions follow the predictions of the AGF model: cells undergo apical constrictions along tensile stress lines oriented along the anteroposterior axis rather than a purely nearest neighbor mechanical interaction (*Figure 15*). These results suggest that the ratchetted apical constrictions of the slow phase of VFF are part of a higher order of organization spanning the entire VF primordium rather than a cellular constriction system based on initial seeds of constriction that initiate nearest neighbor constriction interactions.
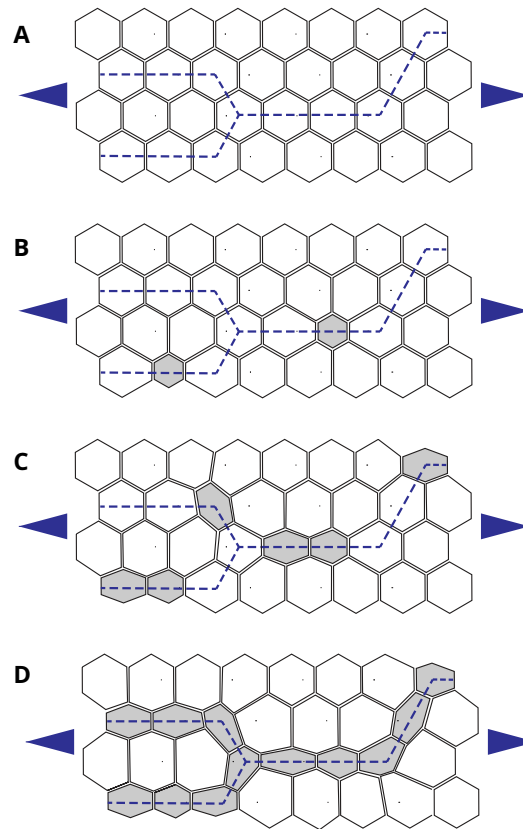
Figure 15. Model for tensile stress-propagated apical constrictions in the early ventral furrow primordium. (**A**) The specified VF primordium is a mechanically active tissue under regional tensile stress from the adjacent anterior and posterior ends containing constricted cells (arrowheads, blue). Example lines of tensile stress (dashed lines, blue) in the tissue before apical constrictions begin. (**B**) Early ratchetted apical constrictions (gray) are distributed along the lines of tensile stress, but do not appear connected. (**C**) A later timepoint showing more apical constrictions (gray) forming along the lines of tensile stress. (**D**) The VF primordium before the fast phase of rapid apical constrictions initiated by the Fog and T48 signaling pathways. Apical constrictions are visible in chains (CCCs).

552   Our theoretical studies showed that tensile stress through the mesoderm primordium at the
553 end of the slow apical constriction phase is primarily carried by the network of CCCs. Moreover, the
554 regions of unconstricted cells between CCCs generally form areas of low stress (as shown by the
555 stress distribution depicted in *Figure 8*). We expect that the reduced cellular stress is conducive for
556 the later Fog and T48 signaling-mediated rapid constriction of the VF placode preceding invagination.
557 It is possible that the unconstricted cells in the low stress pockets are able to constrict with less
558 resistance and at a lower energy cost, as compared with one in an uncorrelated system with no
559 mechanical feedback. Further support for our contention that tensile stress is oriented along the
560 CCCs comes from the observation that CCCs can still propagate across VF primordium regions of
561 experimentally reduced actomyosin contractility in accordance with the predictions of our model.
562   It is likely that the formation of a network of CCCs carrying strong tensile stress oriented along
563 the anterior-posterior axis provides a useful mechanical coupling between different sections of the
564 forming furrow. We anticipate that such a coupling is essential for achieving a uniform invagination
565 when the cell layer buckles inwards, because distortions that may form along the furrow are evened
566 out by the forces associated with the tensile stress. This mechanism is analogous to the one by
567 which a deformed ribbon is straightened out when pulled by its ends. We further propose that
568 mechanical feedback serves to increase robustness of the apical constriction process involved in

initializing VF invagination. The above discussion indicates that CCC morphology and the associated stress distribution, both aided by mechanical feedback during the initial slow phase of apical constrictions, play an important role in achieving well organized and robust VFF. The robustness of the process in response to experimental perturbation has been shown in both the work of *Guglielmi et al.* (*2015*), our analysis of it, and in other recent reports (*Chanet et al., 2017*; *Yevick et al., 2019*). Mechanical processes that are involved in subsequent stages of VFF will be the subject of future studies.

Other morphogenetic phenomena are likely mechanically coordinated in similar ways. Cell intercalation can act to simultaneously narrow a tissue in one dimension and lengthen it in another. During Drosophila germband extension, cells intercalate through polarized actomyosin contraction and subsequent cellular interface shortening to exchange neighboring cells either in a single cell-single cell intercalation or in multicellular interactions through the formation of polarized supracellular actomyosin cables (*Bertet et al., 2004*; *Zallen and Wieschaus, 2004*; *Blankenship et al., 2006*; *Clément et al., 2017*) . Some vertebrate embryonic tissues also undergo convergent extension involving pulsed actomyosin contractions (*Keller et al., 2008*; *Skoglund et al., 2008*; *Rolo et al., 2009*; *Zhou et al., 2009*) . Like VFF apical constrictions, convergent extension might be coordinated by mechanical interactions.

In another embryonic process in Drosophila, dorsal closure, epidermal tissue spreads over another tissue. This process involves apical constriction of the cells of the underlying amnioserosa in addition to the contraction of a supracellular actomyosin cable in the spreading tissue, in addition to other mechanisms (*Martin, 2010*). The amnioserosa is under tension and cells undergo apical constrictions associated with pulsatile actomyosin contractions (*Ma et al., 2009*; *Solon et al., 2009*; *Franke et al., 2005*) .

Tissue level tension has been shown to affect the orientation of mitosis in cell division. This has been observed in certain groups of cells dividing in the extending germband (*Wang et al., 2017*). Tension caused by supracellular actomyosin cables along the Drosophila embryonic parasegmental compartment boundaries orients cell division polarity (*Scarpa et al., 2018*). Likewise, tension generated by actomyosin contractility overrides the general tendency for cell division primarily along the axis of tissue elongation was observed in the follicle cells surrounding the oocyte (*Finegan et al., 2019*). Beyond a direct effect on the mechanical aspects of morphogenetic processes, mechanical deformation and mechanical feedback can regulate gene expression. This has been clearly demonstrated in ventral furrow formation and there is also evidence of the involvement of mechanical feedback mechanisms in a variety of other organisms (*Farge, 2003*; *Pouille et al., 2009*; *Eroshkin and Zaraisky, 2017*) .

Methods

Experimental methods

Immunofluorescence imaging

Drosophila melanogaster embryos were fixed using the heat/methanol protocol (*Miller et al., 1989*). Fixed embryos were stained with mouse anti-Nrt (1:10, Developmental Studies Hybridoma Bank, DSHB), rabbit anti-Zip (*Chougule et al., 2016*) and Hoechst dye. Secondary antibodies used were goat anti-mouse Alexa Fluor 488 (Invitrogen) and goat anti-rabbit Alexa Fluor 546 (Invitrogen). Embryos were mounted in Aquapolymount (Polysciences). Embryos imaged in the mid-sagittal plane were manually oriented (*Spencer et al., 2015*), and embryos imaged in cross-section were manually sectioned (*Thomas and Wieschaus, 2004*). Imaging was performed with a Nikon Ti-E microscope with an A1 confocal system.

Acquiring images of live embryos

Flies and embryos were cultured at 22.5°C. Embryos carrying the *Spider-GFP* transgene (*Morin et al., 2001*) were used to visualize the plasma membrane and cells shape. Embryos were prepared as

Manuscript submitted to eLife

617 described previously (*Gao et al., 2016*; *Martin et al., 2009*; *Cavey and Lecuit, 2008*; *Spencer et al.,*
618 *2015*). Embryos were hand-selected for the optimum stage (early stage 5 (*Wieschaus and Nüsslein-*
619 *Volhard, 1998*)) of development in halocarbon oil 27 (Sigma). The oil was removed by moving the
620 embryos onto agar and then mounting them with glue in embryo chambers designed to avoid
621 compression artifacts (*Gao et al., 2016*). The ventral sides of the embryos were imaged using a 40x
622 oil objective (NA 1.3) of a Nikon Ti-E microscope with an A1 confocal system using a pinhole size of
623 1.6 AU and 4x averaging. Images were collected in three planes separated by 1 μm, at 15 second
624 intervals.

Image processing

626 The following procedure is used to generate the processed confocal microscopy images presented
627 and analyzed in this article. Time lapses of live embryos are loaded into the Embryo Development
628 Geometry Explorer (EDGE) software package for segmentation and tracking (*Gelbart et al., 2012*).
629 EDGE uses a combination of MATLAB routines to distinguish cellular membranes and then identifies
630 cells by drawing an overlay to segment individual frames. This segmentation is an automated
631 process based on user entered variables; however, corrections of the resulting overlay are often
632 necessary and must be done manually. Cells are then tracked using polygon matching by comparing
633 relative centroid location and fractional area overlap between images.

634 After segmentation and tracking have been completed, data is extracted from EDGE in the form
635 of matrices that map the pixels of each frame to individual cells. These pixel matrices are used to
636 identify and tag constricted cells. Tracked cells are marked as constricted based on their minor
637 axis length (MAL) reduction relative to their reference MAL, see *Equation 1*. MALs are calculated
638 from the pixel matrices by solving for the eigenvalues of each cell's second moment matrix. Second
639 moment matrix of cell i is defined by,

$$\boldsymbol{M}_i = \sum_j \begin{bmatrix} (p_{xj} - r_x)^2 & (p_{xj} - r_x)(p_{yj} - r_y) \\ (p_{xj} - r_x)(p_{yj} - r_y) & (p_{yj} - r_y)^2 \end{bmatrix}, \tag{9}$$

640 where (p_{xj}, p_{yj}) are indices of pixel j contained in the discrete array of pixels that describes cell i,
641 and (r_x, r_y) are the indices of the pixel which corresponds with cell i's centroid. These eigenvalues
642 effectively define the length of major and minor axes as though cellular geometries were projected
643 onto an ellipse. Cell specific reference MALs are established by averaging MAL measurements over
644 15 to 20 sequential frames prior to the onset of apical constrictions. Time zero is then selected
645 as the first frame in a given time lapse that has a cell which remains constricted across multiple
646 subsequent frames when a MAL reduction of 65% is implemented.

647 The pixel matrices are also used to generate the cellular neighbor list necessary for identifying
648 clusters. Cells are identified as adjacent neighbors through an iterative process where each pixel of
649 a given cell is checked to see if it is a primary or secondary neighbor to the pixel of any other cell. A
650 list of constricted cell clusters for each frame is then generated by scanning the neighbor list to
651 discern whether constricted cells are adjacent neighbors to any other constricted cells. The list of
652 clusters allows for statistical measures such as total number of clusters and sizes of clusters to be
653 monitored.

Identification of active cells

655 To compare C_{avg} vs $\%N_c$ of live embryos to our model, we normalize C_{avg} by the number of active
656 cells observed. We identify the number of active cells captured in our experimental images by
657 counting all cells across a given time lapse that experience a MAL that is 85% of their reference MAL
658 or lower.

Theoretical AGF model

Simulation domain

661 In our coarse-grained approach the entire apical cell ends are represented as 2D mechanically
662 coupled stress-responsive active particles that are capable of random constrictions, as described in

Manuscript submitted to eLife

the Results section. The curvature of the cellular layer is neglected, and the region of interest is represented as a planar domain (see Fig. *Figure 4*). To accurately represent the relevant domain of the embryo our full-scale simulations are performed in a square domain with 6,400 closely packed particles. This particle number approximately equals the number of cells in the *Drosophila* embryo during the VFF process.

Boundary conditions

We use the periodic boundary conditions both in the horizontal (anteroposterior) and vertical (dorsoventral) directions x and y. The periodicity in the dorsoventral direction y reflects the approximately cylindrical shape of the embryo. The embryo has anterior and posterior end-caps that are relatively immobile throughout this process. We use the periodic boundary condition in the anteroposterior direction x to approximate the relatively rigid boundary of the end caps while avoiding complexities associated with implementing specific boundary conditions for each cap.

Implicit mesoderm representation

To lower the numerical cost we also use the system with reduced number of inactive cells, in which only a portion of the inactive lateral region is modeled explicitly. The effect of the remaining inactive cells on the behavior of the system is approximated by elastic springs acting upon the cells at the border of the explicit domain (see Fig. *Figure 4*D). The spring constant matches the elastic properties of the replaced lateral domain, determined from full simulations of the entire system of 6,400 cells.

Particle-size distribution

To mimic polydispersity of *Drosophila* cells, the system in the initial state (i.e., before the cell constrictions occur) is a disordered 50%–50% mechanically stable mixture of particles with the diameter ratio $r = 1.1$ (*Gao et al., 2006*). The attractive interactions described by *Equation 3* act only between connected adjacent particles. Since cell intercalation does not occur during the slow phase of VFF, the list of connected neighbors is determined in the initial state using a center-to-center distance criterion, and the list remains unchanged throughout the simulation.

We note that the cell shapes are not explicitly represented in the AGF model. The disk diameter corresponds to the size of a cell in mechanical equilibrium in the absence of mechanical forces exerted by the surrounding cells. The actual cell dimensions in the presence of tensile or compressive forces can be approximately inferred from the extension of the springs that connect a given disk to other disks.

Evaluation of the viral stress

The dimensionless virial stress tensor associated with the forces acting on particle i is evaluated from the standard expression

$$S_{\alpha\beta}(i) = -\frac{1}{2\epsilon} \sum_{j \neq i} r_{ij\alpha} f_{ij\beta}, \tag{10}$$

where $\alpha, \beta = x, y$, $r_{ij\alpha} = r_{i\alpha} - r_{j\alpha}$ is the α component of the relative position of particles i and j, $f_{ij\beta}$ is the β component of the force exerted by particle j on particle i, and the summation is over the interacting neighbors. The stress tensor defined by *Equation 10* is symmetric, because the particles are torque-free. The major (minor) stress is the eigenvalue of the stress tensor with the larger (smaller) magnitude, and the major (minor) axis is the direction of the corresponding eigenvector.

Acknowledgements

References

Bertet C, Sulak L, Lecuit T. Myosin-dependent junction remodelling controls planar cell intercalation and axis elongation. Nature. 2004; 429(6992):667–671.

Blankenship JT, Backovic ST, Sanny JSP, Weitz O, Zallen JA. Multicellular rosette formation links planar cell polarity to tissue morphogenesis. Dev Cell. 2006; 11(4):459–470.

Brouzés E, Farge E. Interplay of mechanical deformation and patterned gene expression in developing embryos. Curr Opin Genet Dev. 2004; 14:367–374.

Cavey M, Lecuit T. Imaging cellular and molecular dynamics in live embryos using fluorescent proteins, vol. 420 of Methods in Molecular Biology. Totowa, NJ: Humana Press Inc.; 2008.

Chanet S, Martin AC. Mechanical Force Sensing in Tissues. In: Engler, A J and Kumar, S , editor. *Mechanotransduction*, vol. 126 of Progress in Molecular Biology and Translational Science Elsevier; 2014.p. 317–352.

Chanet S, Miller CJ, Vaishnav ED, Ermentrout B, Davidson LA, Martin AC. Actomyosin meshwork mechanosensing enables tissue shape to orient cell force. Nat Commun. 2017; 8:15014.

Chougule AB, Hastert MC, Thomas JH. Drak Is Required for Actomyosin Organization During Drosophila Cellularization. G3 (Bethesda). 2016; 6(4):819–828.

Clément R, Dehapiot B, Collinet C, Lecuit T, Lenne PF. Viscoelastic Dissipation Stabilizes Cell Shape Changes during Tissue Morphogenesis. Curr Biol. 2017; 27(20):3132–3142.

van Eeden F, St Johnston D. The polarisation of the anterior-posterior and dorsal-ventral axes during Drosophila oogenesis. Curr Opin Genet Dev. 1999; 9:396–404.

Eroshkin FM, Zaraisky AG. Mechano-sensitive regulation of gene expression during the embryonic development. Genesis. 2017; 55(4):e23026.

Farge E. Mechanical induction of twist in the Drosophila foregut/stomodeal primordium. Curr Biol. 2003; 13(16):1365–1377.

Farhadifar R, Roeper JC, Algouy B, Eaton S, Juelicher F. The influence of cell mechanics, cell-cell interactions, and proliferation on epithelial packing. Curr Biol. 2007; 17(24):2095–2104.

Finegan TM, Na D, Cammarota C, Skeeters AV, Nádasi TJ, Dawney NS, Fletcher AG, Oakes PW, Bergstralh DT. Tissue tension and not interphase cell shape determines cell division orientation in the Drosophila follicular epithelium. EMBO J. 2019; 38(3):e100072.

Franke JD, Montague RA, Kiehart DP. Nonmuscle myosin II generates forces that transmit tension and drive contraction in multiple tissues during dorsal closure. Curr Biol. 2005; 15(24):2208–2221.

Gao GJ, Blawzdziewicz J, O'Hern CS. Frequency distribution of mechanically stable disk packings. Phys Rev E. 2006; 74(6, 1):061304.

Gao GJJ, Holcomb MC, Thomas JH, Blawzdziewicz J. Embryo as an active granular fluid: stress-coordinated cellular constriction chains. J Phys Condens Matter. 2016; 28(41):414021.

Gelbart MA, He B, Martin AC, Thiberge SY, Wieschaus EF, Kaschube M. Volume conservation principle involved in cell lengthening and nucleus movement during tissue morphogenesis. PNAS. 2012; 109(47):19298–19303.

Gilmour D, Rembold M, Leptin M. From morphogen to morphogenesis and back. Nature. 2017; 541(7637):311–320.

Guglielmi G, Barry JD, Huber W, De Renzis S. An Optogenetic Method to Modulate Cell Contractility during Tissue Morphogenesis. Dev Cell. 2015; 35(5):646–660.

Heer NC, Martin AC. Tension, contraction and tissue morphogenesis. Development. 2017; 144(23):4249–4260.

Heer NC, Miller PW, Chanet S, Stroop N, Dunkel J, Martin AC. Actomyosin-based tissue folding requires a multicellular myosin gradient. Development. 2017; 144(10):1876–1886.

Hufnagel L, Teleman AA, Rouault H, Cohen SM, Shraiman BI. On the mechanism of wing size determination in fly development. PNAS. 2007; 104(10):3835–3840.

Hunter MV, Fernandez-Gonzalez R. Coordinating cell movements in vivo: junctional and cytoskeletal dynamics lead the way. Curr Opin Cell Biol. 2017; 48:54–62.

Huynh JR, St Johnston D. The Origin of Asymmetry: Early Polarisation of Drosophila Germline Cyst and Oocyte. Curr Biol. 2004; 14:R438–R449.

Ip YT, Maggert K, Levine M. Uncoupling gastrulation and mesoderm differentiation in the Drosophila embryo. EMBO J. 1994; 13(24):5826–5834.

Keller R, Shook D, Skoglund P. The forces that shape embryos: physical aspects of convergent extension by cell intercalation. Phys Biol. 2008; 5(1):015007.

Kondic L, Goullet A, O'Hern CS, Kramar M, Mischaikow K, Behringer RP. Topology of force networks in compressed granular media. EPL. 2012; 97(5):54001.

Krajcovic MM, Minden JS. Assessing the Critical Period for Rho Kinase Activity During Drosophila Ventral Furrow Formation. Dev Dyn. 2012; 241(1):1729–1743.

Ladoux B, Mége RM. Mechanobiology of collective cell behaviours. Nat Rev Mol Cell Biol. 2017; 18(12):743–757.

Leptin M. twist and snail as positive and negative regulators during Drosophila mesoderm development. Genes Dev. 1991; 5(9):1568–1576.

Leptin M. Gastrulation in Drosophila: the logic and the cellular mechanisms. EMBO J. 1999; 18(10):3187–3192.

Leptin M, Grunewald B. Cell-Shape Changes During Gastrulation in Drosophila. Development. 1990; 110(1):73–84.

Ma X, Lynch HE, Scully PC, Hutson MS. Probing embryonic tissue mechanics with laser hole drilling. Phys Biol. 2009; 6(3):036004.

Mammoto T, Ingber DE. Mechanical control of tissue and organ development. Development. 2010; 137(9):1407–1420.

Martin AC. Pulsation and stabilization: contractile forces that underlie morphogenesis. Dev Biol. 2010; 341(1):114–125.

Martin AC, Gelbart M, Fernandez-Gonzalez R, Kaschube M, Wieschaus EF. Integration of contractile forces during tissue invagination. J Cell Biol. 2010; 188(5):735–749.

Martin AC, Kaschube M, Wieschaus EF. Pulsed contractions of an actin-myosin network drive apical constriction. Nature. 2009; 457(7228):495–499.

Miller CJ, Davidson LA. The interplay between cell signalling and mechanics in developmental processes. Nat Rev Genet. 2013; 14(10):733–744.

Miller KG, Field CM, Alberts BM. Actin-binding proteins from Drosophila embryos: a complex network of interacting proteins detected by F-actin affinity chromatography. J Cell Biol. 1989; 109(6 Pt 1):2963–2975.

Mitrossilis D, Röper JC, Le Roy D, Driquez B, Michel A, Ménager C, Shaw G, Le Denmat S, Ranno L, Dumas-Bouchiat F, Dempsy NM, Farge E. Mechanotransductive Cascade of Myo-Ii-Dependent Mesoderm and Endoderm Invaginations in Embryo Gastrulation. Nat Commun. 2017; 8:14188.

Morin X, Daneman R, Zavortink M, Chia W. A protein trap strategy to detect GFP-tagged proteins expressed from their endogenous loci in Drosophila. PNAS. 2001; 98(26):15050–15055.

Pouille PA, Ahmadi P, Brunet AC, Farge E. Mechanical Signals Trigger Myosin II Redistribution and Mesoderm Invagination in Drosophila Embryos. Sci Signal. 2009; 2(66):ra16.

Riechmann V, Ephrussi A. Axis formation during Drosophila oogenesis. Curr Opin Genet Dev. 2001; 11:374–383.

Rolo A, Skoglund P, Keller R. Morphogenetic movements driving neural tube closure in Xenopus require myosin IIB. Dev Biol. 2009; 327(2):327–338.

Scarpa E, Finet C, Blanchard GB, Sanson B. Actomyosin-Driven Tension at Compartmental Boundaries Orients Cell Division Independently of Cell Geometry In Vivo. Dev Cell. 2018; 47(6):727–740.

796 **Seher TC**, Narasimha M, Vogelsang E, Leptin M. Analysis and reconstitution of the genetic cascade controlling
797 early mesoderm morphogenesis in the Drosophila embryo. Mech Dev. 2007; 124(3):167–179.

798 **Skoglund P**, Rolo A, Chen X, Gumbiner BM, Keller R. Convergence and extension at gastrulation require a
799 myosin IIB-dependent cortical actin network. Development. 2008; 135(14):2435–2444.

800 **Solon J**, Kaya-Copur A, Colombelli J, Brunner D. Pulsed forces timed by a ratchet-like mechanism drive directed
801 tissue movement during dorsal closure. Cell. 2009; 137(7):1331–1342.

802 **Spencer AK**, Siddiqui BA, Thomas JH. Cell shape change and invagination of the cephalic furrow involves
803 reorganization of F-actin. Dev Biol. 2015; 402:192–207.

804 **St Johnston D**, Nüsslein-Volhard C. The Origin of Pattern and Polarity in the Drosophila Embryo. Cell. 1992;
805 68:201–219.

806 **Sweeton D**, Parks S, Costa M, Wieschaus E. Gastrulation in *Drosophila*: the formation of the ventral furrow and
807 posterior midgut invaginations. Development. 1991; 112:775–789.

808 **Thomas JH**, Wieschaus E. src64 and tec29 are required for microfilament contraction during Drosophila
809 cellularization. Development. 2004; 131(4):863–871.

810 **Tordesillas A**, Tobin ST, Cil M, Alshibli K, Behringer RP. Network flow model of force transmission in unbonded
811 and bonded granular media. Phys Rev E: Stat Nonlinear Soft Matter Phys. 2015; 91(6):062204.

812 **Wang MF**, Hunter MV, Wang G, McFaul C, Yip CM, Fernandez-Gonzalez R. Automated cell tracking identifies
813 mechanically oriented cell divisions during Drosophila axis elongation. Development. 2017; 144(7):1350–1361.

814 **Weng M**, Wieschaus E. Myosin-dependent remodeling of adherens junctions protects junctions from Snail-
815 dependent disassembly. J Cell Biol. 2016; 212(2):219–229.

816 **Wieschaus EP**, Nüsslein-Volhard C. Looking at embryos. In: Roberts DB, editor. *Drosophila: A Practical Approach*,
817 2 ed. Oxford, England: Oxford University Press; 1998.p. 179–214.

818 **Xie S**, Martin AC. Intracellular signalling and intercellular coupling coordinate heterogeneous contractile events
819 to facilitate tissue folding. Nat Commun. 2015; 6:7161.

820 **Yevick HG**, Pearson WM, Dunkel J, Martin AC. Structural Redundancy in Supracellular Actomyosin Networks
821 Enables Robust Tissue Folding. Dev Cell. 2019; doi: 10.1016/j.devcel.2019.06.015.

822 **Zallen JA**, Wieschaus E. Patterned gene expression directs bipolar planar polarity in Drosophila. Dev Cell. 2004;
823 6(3):343–355.

824 **Zhang H**, Labouesse M. Signalling through mechanical inputs - a coordinated process. J Cell Sci. 2012;
825 125(13):3039–3049.

826 **Zhou J**, Kim HY, Davidson LA. Actomyosin stiffens the vertebrate embryo during crucial stages of elongation
827 and neural tube closure. Development. 2009; 136(4):677–688.